JOURNAL OF GEOPHYSICAL RESEARCH, VOL. ???, XXXX, DOI:10.1029/,

Broad-band ambient noise surface wave tomography across the United States

G. D. Bensen

Center for Imaging the Earth's Interior, Department of Physics, University of Colorado at Boulder, Boulder, Colorado USA

M. H. Ritzwoller

Center for Imaging the Earth's Interior, Department of Physics, University of Colorado at Boulder, Boulder, Colorado USA

N. M. Shapiro

Laboratoire de Sismologie, CNRS, IPGP, Paris, France

G. D. Bensen, Department of Physics, University of Colorado at Boulder, Campus Box 390, Boulder, CO 80309, USA. (gbensen@colorado.edu)

Abstract.

This study presents surface wave dispersion maps across the contiguous United States determined using seismic ambient noise. Two years of ambient noise are used from March 2003 through February 2005 observed at nearly 200 broad-band seismic stations in the US, southern Canada, and northern Mexico. Cross-correlations are computed between all station-pairs to produce empirical Green functions. At most azimuths across the US, coherent Rayleigh wave signals exist in the empirical Green functions implying that ambient noise in the frequency band of this study (5 - 100 sec period) is sufficiently isotropically distributed in azimuth to yield largely unbiased dispersion measurements. Rayleigh and Love wave group and phase velocity curves are measured together with associated uncertainties determined from the temporal variability of the measurements. A sufficient number of measurements (>2000) is obtained between 8 sec and 25 sec for Love waves and 8 sec and 70 sec for Rayleigh waves to produce tomographic dispersion maps. Both phase and group velocity maps are presented in these period bands. Resolution is estimated to be better than 100 km across much of the US from 8-40 sec period for Rayleigh waves and 8-20 sec period for Love waves, which is unprecedented in a study at this spatial scale . At longer and shorter periods, resolution degrades as the number of coherent signals diminishes. The dispersion maps agree well with each other and with known geological and tectonic features and, in addition, provide new information about structures in the crust and uppermost mantle beneath much of the US.

1. Introduction

The purpose of this study is to produce surface wave dispersion maps across the contiguous United States using ambient noise tomography. We present Rayleigh and Love wave group and phase speed maps and assess their resolution and reliability. These maps display higher resolution and extend to shorter periods than previous surface wave maps that have been produced across the United States using traditional teleseismic surface wave tomography methods. The maps presented form the basis for an inversion to produce a higher resolution 3-D model of V_s in the crust and uppermost mantle, but this inversion is beyond the scope of the present paper.

Surface wave empirical Green functions (EGFs) can be determined from cross-correlations between long time sequences of ambient noise observed at different stations. In places we use the terms cross-correlogram and empirical Green function interchangeably, but they differ by an additive phase factor (e.g., *Lin et al.* [2007a]). Investigations of surface wave empirical Green functions have grown rapidly in the last several years. The feasibility of the method was first established by experimental (e.g., *Weaver and Lobkis* [2001], *Lobkis and Weaver* [2001], *Derode et al.* [2003], *Larose et al.* [2005]) and theoretical (e.g., *Snieder* [2004], *Wapenaar* [2004]) studies. *Shapiro and Campillo* [2004] demonstrated that the Rayleigh wave EGFs estimated from ambient noise possess dispersion characteristics similar to earthquake derived measurements and model predictions. The dispersion characteristics of surface wave empirical Green functions derived from ambient noise have been measured and inverted to produce dispersion tomography maps in several geographical settings, such as Southern California (*Shapiro et al.* [2005];

Sabra et al. [2005]), the western US (*Moschetti et al.* [2007]; *Lin et al.* [2007a]), Europe (*Yang et al.* [2007]), Tibet (*Yao et al.* [2006]), New Zealand (*Lin et al.* [2007b]), Korea (*Cho et al.* [2007]), Spain (*Villasenor et al.* [2007]) and elsewhere. Most of these studies focused on Rayleigh wave group speed measurements obtained at periods below about 20 sec. *Campillo and Paul* [2003] showed that Love wave signals can emerge from cross-correlations of seismic coda and *Gerstoft et al.* [2006] also noticed several signals on transverse-transverse cross-correlations of ambient noise. These studies did not, however, demonstrate the consistent recovery of Love wave signals from ambient noise. *Lin et al.* [2007a] placed both phase speed and Love wave measurements on a firm foundation and showed that Love waves are readily observed using ambient noise. We follow their methodology to present phase velocity and Love wave maps here in addition to group velocity and Rayleigh wave maps. We apply ambient noise tomography on a geographical scale much larger than all previous studies. The larger spatial scale also allows us to extend the results to longer periods than in previous studies.

All of the results presented here are based on the data processing scheme described by *Bensen et al.* [2007]. This method is designed to minimize the negative effects that result from a number of phenomena, such as earthquakes, temporally localized incoherent noise sources, and data irregularities. It also is designed to obtain dispersion measurements to longer periods and along longer inter-station paths than in previous studies, and, thus, increases the band-width and the geographical size of the study region.

Previous surface wave tomography across the North American continent was based on teleseismic earthquake measurements. Several of these studies involved measurements obtained exclusively across North America (e.g., *Alsina et al.* [1996], *Godey et al.* [2003],

van der Lee and Nolet [1997]) whereas others involved data obtained globally (e.g., *Trampert and Woodhouse* [1996]; *Ekström et al.* [1997]; *Ritzwoller et al.* [2002]). Ambient noise tomography possesses complementary strengths and weaknesses to traditional earthquake tomography. Single-station earthquake tomography benefits from the very high signal-to-noise ratio of teleseismic surface waves and the dispersion measurements extend to very long periods (>100 sec) which results in constraints on deep upper mantle structures. Several characteristics limit the power of traditional earthquake tomography, however. First, teleseismic propagation paths make short period (< 20 sec) measurements difficult to obtain in aseismic regions due to the scattering and attenuation that occur as distant waves propagate. This is unfortunate because short period measurements are needed to resolve crustal structures. This is particularly disadvantageous across the US, which exhibits a low level of seismicity in most regions. Second, the long paths also result in broad lateral sensitivity kernels which limits resolution to hundreds of kilometers. Third, dispersion measurements from earthquakes typically have unknown uncertainties. Finally, uncertainties in source location and depth manifest themselves in uncertainties in the "initial phase" of the measurement, which imparts an ambiguity to phase and group speeds measured from earthquakes.

Although the empirical Green functions obtained by cross-correlating long time-series between pairs of stations demonstrate a smaller signal-to-noise ratio than large earthquakes and the resulting ambient noise dispersion measurements typically are limited to periods well below 100 sec, ambient noise tomography improves on each of the shortcomings of traditional earthquake tomography. First, ambient noise empirical Green functions provide dispersion maps to periods down to ∼6 seconds (and lower in some places with

exceptionally dense station spacing), potentially with much better lateral resolution, particularly in the context of continental arrays of seismometers in which path density and azimuthal coverage can be very high. Second, one can estimate uncertainties from the repeatability of ambient noise measurements (e.g., *Bensen et al.* [2007]). Third, the station locations and the "initial phase" of the EGFs are both well known (*Lin et al.* [2007a]), so the measurements tend to be both more precise and more easily interpreted than earthquake signals.

Ambient noise tomography, therefore, provides a significant innovation in seismic methodology that is now yielding new information about the Earth with resolutions near the inter-station spacing. The currently developing Transportable Array component of EarthScope/USArray is being deployed on a rectangular grid and is now being used across the western US for ambient noise tomography by *Moschetti et al.* [2007]. Its traverse across the United States will not complete until the year 2014, however.

This paper is the first continental scale application of ambient noise tomography and is based on nearly 200 permanent and temporary stations throughout the contiguous US and in southern Canada and northern Mexico (Fig. 1a). Rayleigh wave tomography maps are created from 8 to 70 seconds period and Love wave maps from 8 to 25 sec. We present a subset of these maps. These maps provide new information about the crust and mantle beneath the United States, show that the technique is not limited to short periods or regional scales, and add further credibility to ambient noise surface wave tomography.

2. Data Processing

We follow the method described in detail by *Bensen et al.* [2007] for data processing from observations of ambient seismic noise to the production of group velocity measurements.

Phase speed measurements and Love wave data processing follow the procedure of *Lin et al.* [2007a]. We briefly review here the data processing procedure and discuss the repeatability of the dispersion measurements as well as the way in which signal-to-noise ratio (SNR) varies with period and region. In later sections, we discuss how measurements from almost 20,000 inter-station paths are selected to be used for tomographic inversion to estimate group and phase speed dispersion maps (*Barmin et al.* [2001]) ranging from 8 seconds to 70 seconds for Rayleigh waves and 8 to 25 seconds for Love waves. Only a subset of these maps, however, will be shown here.

We processed all available vertical and horizontal component broad-band seismic data from the 200 stations (Fig. 1a) that are available from the IRIS DMC and the Canadian National Seismic Network (CNSN) for the 24-month period from March 2003 through February 2005. Although the data come from this 24-month window, most time-series are shorter than 24-months because of station down time or installation during this period. Time-series lengths are referred to in terms of the time window from which the waveforms derived, but actual time-series lengths vary within the same time window. Station locations are identified in Figure 1a. Station coverage in the west and parts of the eastern mid-west is good, but the north-central US and the near-coastal eastern US are poorly covered. As seen later, this has ramifications for resolution. The azimuthal distribution of inter-station paths is shown in Figure 1b. This includes both inter-station azimuth and back-azimuth, presented as the number of paths falling into each 10° azimuth bin. Large numbers at a particular azimuth (or back-azimuth, both are included) correspond to the dominant inter-station directions. For example, in the eastern and central US, stations are oriented dominantly to pick up waves traveling to the north-east or the west. Concen-

trations of stations, such as in California, tend to produce large numbers of inter-station directions in a narrow azimuthal range. The diagrams are not azimuthally symmetric because azimuth and back-azimuth are not 180°-complements. Figure 1b dominantly reflects the geometry of the seismic network used. Later in the paper, we discuss the directions of propagation of the strongest signals and reference them to the azimuthal distribution of inter-station paths in Figure 1a.

Data preparation is needed prior to cross-correlation. Starting with instrument response corrected day-long time-series at each station, we first perform time-domain normalization to mitigate the effects of large amplitude events (e.g., earthquakes and instrument glitches). Initially, researchers favored a 1-bit (or sign bit, or binary) normalization (*Larose et al.* [2004], *Shapiro et al.* [2005]), but *Bensen et al.* [2007] argued for the application of a temporally variable weighting function to retain more of the small amplitude character of the raw data and to allow for flexibility fin defining the amplitude normalization in particular period bands. Here, we define the temporal normalization weights between periods of 15 and 50 sec, but apply the weights to the unfiltered data. As discussed by *Bensen et al.* [2007], this removes earthquakes from the daily time-series more effectively than defining the temporal normalization on the raw data. The impact is seen most strongly in the quality of the Love wave signals. This procedure is applied to both the vertical and horizontal component data, but the relative amplitudes of the two horizontal components must be maintained. An additional spectral whitening is performed to all of the waveforms for each day to avoid significant spectral imbalance. Again, the same filter must be applied to both horizontal components. Spectral whitening increases the band-width of the automated broad-band dispersion measurements. (*Bensen et al.* [2007] present

more details). After temporal and spectral normalization, cross-correlation is performed on day-long time-series for vertical-vertical, east-east, east-north, north-east, and north-north components. The horizontal components are then rotated to radial-radial (R-R) and transverse-transverse (T-T) orientations as defined by the great circle path between the two stations. These daily results are then "stacked" for the desired length of input (e.g. one month, one year, etc.). The Rayleigh wave (Z-Z and R-R) and Love wave (T-T) cross-correlograms yield two-sided ("causal" and "anticausal") empirical Green functions corresponding to waves propagating in opposite directions between the stations. Both the causal and acausal EGFs are equally valid and can be used as input into the dispersion measurement routine, but may have different spectral content and signal-to-noise ratio characteristics. Both for simplicity and to optimize the band-width of the empirical Green functions, we average the causal and anticausal signals into a single "symmetric signal" from which all dispersion measurements are obtained.

The frequency dependent group and phase velocities from the Rayleigh and Love wave EGFs are estimated using an automated dispersion measurement routine. Following *Levshin et al.* [1972], we performed Frequency-Time Analysis (FTAN) to measure the phase and group velocity dispersion on all recovered signals. The FTAN technique applies a sequence of Gaussian filters at a discrete set of periods and measures the group arrival times on the envelope of these filtered signals. Phase velocity is also measured and further details can be found in *Lin et al.* [2007a]. We used the 3D model of *Shapiro and Ritzwoller* [2002] to resolve the 2π phase ambiguity, which was successful in the vast majority of cases. The Rayleigh and Love wave signals apparent on the empirical Green functions are less complicated than earthquake signals because the inter-station path lengths are

relatively short and the absence of body waves simplifies the signal. This allowed the automation of the dispersion measurements. Selected examples of the symmetric component Rayleigh wave waveforms and the resulting group and phase speed measurements are shown in Figure 2a,b. The broad-band dispersive nature of these waveforms is seen in Figure 2a with longer period energy arriving first. Figure 2b shows the resulting group and phase dispersion curves. The fastest path lies between stations GOGA (Godrey, GA, USA) and VLDQ (Val d'Or, Quebec, Canada) in the tectonically stable part of eastern North America. The slowest path is between stations DUG (Dugway, AR, USA) and ISA (Isabella, CA, USA) in the tectonically active part of the western US. The other two paths (Camsell Lake, NWT, Canada to Albuquerque, NM, USA; Cathedral Cave, MO, USA to Whiskeytown Dam, CA, USA) have intermediate speeds and propagate through a combination of tectonically deformed and stable regions.

Examination of the Rayleigh and Love wave signals reveals the difference between the speeds and signal strengths. Figure 3 presents examples of Z-Z, R-R, and T-T EGFs in the period range from 5 to 50 sec. Figure 3a contains the empirical Green functions between stations CCM (Crystal Cave, MO, USA) and RSSD (Black Hills, SD, USA) with an interstation distance of 1226 km. Rayleigh waves are seen on the vertical-vertical (Z-Z) and radial-radial (R-R) cross-correlograms and arrive at similar times. Love wave signals are seen on the transverse-transverse (T-T) cross-correlograms. The different Rayleigh and Love wave arrival times are clear and are identified with different velocity windows in the diagram. Figure 3b,c present record sections for the Z-Z and T-T cross-correlograms from the 13 Global Seismic Network (GSN) stations (*Butler et al.* [2004]) in the study region.

Approximate move-outs of 3.0 and 3.3 km/sec for Rayleigh and Love waves are shown in Figures 3b and 3c, respectively.

3. Data Selection

After the empirical Green functions are computed between every station-pair for the Z-Z and T-T components, several selection criteria are applied prior to tomography. The effect of each step of the process in reducing the data set is indicated in Tables 1 and 2.

First, we apply a minumum three wavelength inter-station distance constraint, which is imposed because of measurement instabilities at shorter distances and to be in accord with the far-field approximation (*Levshin et al.* [1999]; *Snieder* [2004]). This criterion significantly reduces the number of measurements at periods above 50 seconds because stations must be separated by more than 600 km.

Second, we apply a selection criterion based on the period-dependent signal-to-noise ratio (SNR), which is defined as the peak signal in a signal window divided by the root-mean-square (RMS) of the trailing noise, filtered with a specified central period. Average SNR values for the Z-Z, R-R, and T-T EGFs are seen in Figure 4. A dispersion measurement is retained at a period only if the SNR > 15 for the cross-correlogram at that period.

Similarities in the patterns of SNR as a function of period for Rayleigh waves on the Z-Z and R-R components are observed in Figure 4 up to 20 seconds period; although the R-R signal quality is lower. Above 20 sec, the R-R SNR degrades more quickly, however, similar to the trend of the SNR for the T-T cross-correlations. This pattern is consistent with the results of *Lin et al.* [2007a]. Apparently, the SNR degrades at longer periods predominantly due to increasing levels of incoherent local noise, and may not be

due to decreasing signal levels. Because the SNR is much higher on the Z-Z than the R-R components and the Z-Z band-width is larger, we only use Rayleigh wave dispersion measurements obtained on the Z-Z cross-correlations.

Figure 5 presents information about the geographical distribution of signal quality. The average SNR of all waveforms is shown for Rayleigh (Z-Z) and Love (T-T) wave signals in each of the four regions defined in Figure 1a where both stations lie within the sub-region. SNR in the sub-regions is higher than over the entire data set (Fig. 4) because path lengths are shorter, on average, by more than a factor of two in the regional data. Rayleigh wave SNR is highest in the south-west region, with SNR in the other regions being lower but similar to each other. Long period SNR, in particular, is considerably higher in the south-west than in other regions. In most regions, the Rayleigh wave curves show double peaks apparently related to the primary and secondary microseism periods of 15 and 7.5 sec, respectively.

For Love waves, the highest SNR is in the south-west and north-west regions and the curves display only a single peak near the primary microseismic band, peaking in different regions between 13 and 16 sec period. The strongest Love waves are in the north-west, unlike the Rayleigh waves which are strongest in the south-west region. Thus, the distribution of Rayleigh and Love wave energies differ and they may not be co-generated everywhere. Although Figure 4 shows that below 15 sec period Love waves have a higher SNR than Rayleigh waves, this is true only in the western US. In the central and eastern US, Rayleigh and Love waves below about 15 sec have similar strengths. In all regions, Love wave signals are negligible above about 25 sec period. Love waves are much stronger in the western US than in the central or eastern US, particularly above about 15 sec

period. These results indicate clearly that the strongest ambient noise sources are located generally in westerly directions, although substantial Rayleigh wave signal levels also exist in the central and eastern US, Love waves in the central and eastern US, however, are much weaker above about 15 sec.

Third, we apply a data selection criterion based on the variability of measurements repeated on temporally segregated subsets of the data. We compiled cross-correlations for overlapping 6-month input time-series (e.g. June, July, August 2003 plus June, July, August 2004) to obtain 12 "seasonal" stacks. We measure the dispersion curves on data from each 6-month (dual 3-month) time window and on the complete 24-month time window. For each station-pair, the standard deviation of the dispersion measurements is computed at a particular period using data from all of the 6-month time windows in which SNR > 10 at that period. An illustration of this procedure appears in Figure 6. Figure 6a shows the Z-Z, R-R, and T-T EGFs used from the 2685 km path between stations DWPF (Disney Wilderness Preserve, FL, USA) and RSSD (Black Hills, SD, USA). Figure 6b,c,d compares the measurements obtained on the 6-month temporal subsets of data with the 24-month group and phase velocity measurements. The error bars indicate the computed standard deviation. If fewer than four 6-month time-series satisfy the criterion that SNR > 10, then the standard deviation of the measurement is considered indeterminate and we assign three times the average of the standard deviations taken over all measurements within the data set. The average standard deviation values are shown in Figure 7. Finally, we reject measurements for a particular wave type (Rayleigh/Love, group/phase speed) and period if the estimated standard deviation is greater than 100 meters/sec, as this

indicates an instability in the measurement. The inverse of the standard deviation is used as a weight in the tomographic inversion (e.g., *Barmin et al.* [2001]).

In contrast with Figure 7, Figure 8 contains the mean measurement standard deviation values for each of the four sub-regions defined in Figure 1a. The measurements are labeled for Rayleigh and Love wave group and phase measurements. The patterns are similar for all sub-regions. Because dramatic differences between measurement uncertainties in different regions are not observed, similar measurement quality is obtained in all regions even though there are differences between the regions in average SNR and, therefore, different numbers of measurements in each region. The most stable measurements are Rayleigh wave phase speeds, particularly above about 20 sec where phase speed is more robust than group speed. Below 20 sec period, the envelope on which group velocity is measured becomes narrower at short periods and increases measurement precision. Thus, the accuracy of the group velocity measurements becomes similar to the phase velocity measurements below 20 sec period. Although the Love wave phase velocity measurements have favorable standard deviation with increasing period, the number of high quality measurements above 20 sec period drops precipitously due to low signal levels. Finally, as a rule-of-thumb, at periods above about 30 sec, the standard deviation of Rayleigh wave phase speed measurements is about half that of group speed.

Fourth, we apply a final data selection criterion based on tomographic residuals. Using the thus far accepted measurements, we create an overly-smoothed tomographic dispersion map for each wave type (Rayleigh/Love, group/phase velocity). Measurements for each wave type with high travel time residuals (three times the root-mean-squared residual value at a given period and wave type) are removed and the overly smoothed disper-

sion map is recreated, becoming the background dispersion map for the later finer-scale inversion.

The final Rayleigh wave (Z-Z) path retention statistics for selected periods are shown in Table 1. Similar statistics for Love waves (T-T) at periods of 10, 16 and 25 seconds period are shown in Table 2. The number of paths retained at periods above about 70 sec for Rayleigh waves and 25 sec for Love waves is insufficient for tomography across the US, but the longer period measurements are useful in combination with teleseismic dispersion measurements.

4. Azimuthal distribution of signals

The theoretical basis for surface wave dispersion measurements obtained on ambient noise and the subsequent tomography assumes that ambient noise is distributed homogeneously with azimuth (e.g., *Snieder* [2004]). Asymmetric two-sided cross-correlograms, such as those in Figure 3a and documented copiously elsewhere (e.g., *Stehly et al.* [2006]), illustrate that the strength and frequency content of ambient noise varies appreciably with azimuth. This motivates the question as to whether ambient noise is well enough distributed in azimuth to return unbiased dispersion measurements for use in tomography. *Lin et al.* [2007a] present evidence, based on measurements of the "initial phase" of phase speed measurements from a three-station method, that in the frequency band they consider (6 - 40 seconds period) ambient noise is distributed sufficiently isotropically so that phase velocity measurements are returned largely unbiased. Another line of evidence that supports the robustness of the dispersion measurements derived from ambient noise comes from the variability of the dispersion measurements, as the directional content of ambient noise varies between seasons. This is, of course, the basis for our error analysis.

Here, we take another approach, and attempt to map the direction of propagation of relatively large amplitude signals. We are not interested exclusively in the directions from which the largest amplitude signals emanate, which have interested researchers who aim to understand the strongest sources of ambient noise (e.g., *Stehly et al.* [2006]). Rather, we are interested in the directions of propagation of all coherent signals that rise above background incoherent noise because these signals form the basis for the ambient noise tomographic method. In this assessment, the distribution of paths dictated by the geometry of the array must be borne in mind. Consequently, all results are taken relative to the azimuthal distributions presented in Figure 1b.

Figure 9 presents the azimuthal distribution of large amplitude Rayleigh wave signals at periods of 8, 14, 25 and 40 sec. Our measurements are divided into three sub-regions as defined in Figure 1a, but with the central and eastern regions combined. Only one station in each station-pair is required to be in a sub-region. Both azimuth and back-azimuth are included in the figure. Averaging over all regions and azimuths, at periods of 8, 14, 25, and 40 sec the fraction of Rayleigh wave EGFs with a SNR>10 is 0.38, 0.49, 0.54 and 0.38, respectively, and reduces quickly for periods above 40 sec. To compute this fraction as a function of azimuth, the number of paths with SNR > 10 in a given $20/circ$ azimuth bin is divided by the total number of paths in that bin given by Figure 1b. The SNR on both cross-correlation lags is considered separately, and the indicated azimuth is the direction of propagation. We refer to the positive and negative lag contributions as having come from different "paths" for simplicity, but, in fact, the paths are the same and only the azimuths differ.

Inspection of Figure 9 reveals that the fraction of relatively high SNR paths at a given azimuth is fairly homogeneously distributed with azimuth. At 14 sec and 25 sec period, in all three regions all azimuths have the fraction of paths with SNR >10 above 20% and, hence, the distribution of useful ambient noise signals is fairly homogeneous, even though the highest SNR signals may arrive from only a few principal directions. At 8 seconds period, the results are not as geographically consistent. In the two western regions, the strongest signals are those with noise coming from the west. This agrees with the notion that these results would be dominated by the 7.5 sec period secondary microseism. In the east and central regions, however, signals come both from the west and northeast and there are fewer high SNR cross-correlations. Finally, moving to 40 sec period, the overall fraction of high SNR measurements is lower. Relative to this lower level, the azimuthal distribution again has a homogeneous component although certain azimuths have a higher fraction of high SNR paths. The azimuthal pattern above 40 sec in each region remains about the same as at 40 sec, but the fraction of high SNR observations diminishes rapidly.

In conclusion, therefore, at all periods, in all regions and most azimuths, coherent Rayleigh wave signals exist in ambient noise. This is least true at periods below 10 sec, where most of the Rayleigh wave energy is coming generally from the west, but even in this case the well sampled azimuths cover nearly 180 degrees. This observation provides another item in a growing list of evidence indicating that ambient noise in this frequency band is sufficiently isotropically distributed in azimuth to yield largely unbiased dispersion measurements.

5. Tomography

An extensive discussion of the tomography procedure is presented in *Barmin et al.* [2001]. We follow their discussion to provide a basic introduction to the overall procedure and define some needed terms. The tomographic inversion is a 2-D ray theoretical method, similar to a Gaussian beam technique and assumes wave propagation along a great circle but with "fat" rays. Starting with observed travel times we estimate a model $\mathbf{m}$ (2-D distribution of surface wave slowness) by minimizing the penalty functional:

$$(\mathbf{G}(\mathbf{m}) - \mathbf{d})^T \mathbf{C}^{-\mathbf{1}} (\mathbf{G}(\mathbf{m}) - \mathbf{d}) + \alpha^2 \|F(\mathbf{m})\|^2 + \beta^2 \|H(\mathbf{m})\|^2, \quad (1)$$

where $\mathbf{G}$ is the forward operator computing travel times from a model, $\mathbf{d}$ is the data matrix of measured surface wave travel times, and $\mathbf{C}$ is the data covariance matrix assumed here to be diagonal and composed of the square of the measurement standard deviations. F($\mathbf{m}$) is the spatial smoothing function where

$$F(\mathbf{m}) = m(\mathbf{r}) - \int_S S(\mathbf{r}, \mathbf{r}') m(\mathbf{r}') d\mathbf{r}', \quad (2)$$

and

$$S(\mathbf{r}, \mathbf{r}') = K_0 \exp(-\frac{|\mathbf{r} - \mathbf{r}'|^2}{2\sigma^2}) \quad (3)$$

where

$$\int_S S(\mathbf{r}, \mathbf{r}') d\mathbf{r}' = 1, \quad (4)$$

and $\mathbf{r}$ is the target location and $\mathbf{r}'$ is an arbitrary location The function H penalizes the model in regions with poor path or azimuthal coverage. The contributions of H and F are controlled by the damping parameters α and β while spatial smoothing (related to the fatness of the rays) is controlled by adjusting σ. These three parameters (α, β and σ) are user controlled variables that are determined through trial and error optimization.

The resulting spatial resolution is found at each point by fitting a 2-D Gaussian function to the resolution matrix (map) defined as follows:

$$A \exp(-\frac{|\mathbf{r}|^2}{2\gamma^2}) \tag{5}$$

where $\mathbf{r}$ here denotes the distance from the target point. The standard deviation of the Gaussian function, γ, is useful for understanding the spatial size of the features that can be determined reliably in the tomographic maps. In this paper, we report 2γ as the resolution, the full-width of the resolution kernel at each point. Figure 10a shows the resolution map for the 10 sec Rayleigh wave group speed. The corresponding ray coverage is shown in Figure 10b. The more densely instrumented regions, such as southern California and near the New Madrid shear zone in the central United States, have resolution <70 km, which is better than the inter-station spacing in these regions. Across most of the US, resolution averages about 100 km for Rayleigh waves up to 40 sec and then degrades to 200 km at 70 sec period. For Love waves, resolution averages about 130 km below 20 sec, but then rapidly degrades at longer periods so that at 20 sec the average resolution is about 200 km. The rapid degradation of average resolution in the US for Love waves is due to the loss of Loves wave signals in the eastern US, which sets on at about 15 sec, as discussed above. Regions with resolution worse than 1000 km are indicated on the tomographic maps in grey and, in addition, to outline the high resolution regions we plot the 200 km resolution contours.

We use ray theory as the basis for tomography in this study, albeit with "fat rays" given by the correlation length parameter σ. In recent years, surface wave studies have increasingly moved toward diffraction tomography using spatially extended finite-frequency sensitivity kernels based on the Born/Rytov approximation (*Spetzler et al.* [2002]; *Ritzwoller*

et al. [2002]; *Yoshizawa and Kennett* [2002]; and many others). *Ritzwoller et al.* [2002] showed that ray theory with fat rays produces similar structure to diffraction tomography in continental regions at periods below 50 seconds and the similarities strengthen as path lengths decrease. *Yoshizawa and Kennett* [2002] argued that the spatial extent of sensitivity kernels is effectively much less than given by the Born/Rytov theory, being confined to a relatively narrow "zone of influence" near the classical ray. They conclude, therefore, that in many applications, off-great-circle propagation may provide a more important deviation from straight-ray theory than finite frequency effects. *Ritzwoller and Levshin* [1998] show that off-great-circle propagation can be largely ignored at periods above about 30 seconds for paths with distances less than 5000 km, except in extreme cases. From a practical perspective then, these arguments support the contention that ray-theory with ad-hoc fat rays can adequately represent wave propagation for most of the path lengths and most of the period range under consideration here. A caveat is for relatively long paths (>1000 km) at short periods (<20 sec), in which case off-great-circle effects may become important. Off-great-circle effects will be largest near structural gradients, but are mitigated by observations made on orthogonal paths. In our study region, where structural gradients are largest azimuthal path coverage tends to be quite good. These considerations lead us to believe that ray theory with fat-rays is sufficient to produce meaningful dispersion maps and that uncertainties in the maps produced by the arbitrariness of the choice of the damping parameters are probably larger than errors induced by the simplified theory. Nevertheless, future work is called for to test this assertion and to quantify how fully modeling off great-circle propagation would change the maps. We anticipate only subtle changes.

6. Results

In this section we present examples of the tomographic maps with the particular purpose of establishing their credibility and limitations. In the next section, we qualitatively discuss some of the structural features that appear in the maps.

This tomography method is applied to the final set of accepted measurements to produce dispersion maps from 8 to 70 sec period for Rayleigh waves and 8 to 25 sec period for Love waves. In this period range more than 2000 measurements exist for all wave types. The method is applied on a $0.5^\circ \times 0.5^\circ$ geographical grid across the study region. Examples of the resulting dispersion maps are presented in Figures 11 - 14. In all maps, the 200 km resolution contour is shown with a thick black or grey contour and the grey regions are those areas on the continent that have indeterminate velocities. The damping parameters α and β in equation (1) which control the strength of the smoothness constraint and the tendency of the inversion to stay at the input model are determined subjectively to supply acceptable fit to the data, while retaining the coherence of large-scale structures and controlling the tendency of streaks and stripes to contaminate the maps. The smoothing or correlation length parameter, σ, is chosen to be 125 km at periods below 25 sec and 150 km at longer periods. As with any tomographic inversion, the resulting maps are not unique but the features that we discuss below are common to any reasonable choice of the damping and smoothness parameters.

Discussion of the tomographic maps is guided by the vertical V_s sensitivity kernels shown in Figure 15. At a given period, phase velocity measurements tend to sense deeper structures than group velocity measurements and Rayleigh waves sense deeper than Love

waves. Thus, at any period the Rayleigh wave phase velocities will have the deepest sensitivity and the Love wave group velocities will be most sensitive to shallow structures.

Figures 11 and 12 show Rayleigh and Love wave group and phase speed maps at 10 and 20 sec period, respectively. Sedimentary thickness contours are over-plotted in Figure 11 and will be discussed further in the next section. The 10 sec maps are all similar to one another, with much lower speeds in the western than the eastern US. The similarity of the maps is expected because these wave types are all predominantly sensitive to crustal structures, notably the existence of sediments. Thus, the principal features on these maps are slow anomalies correlated with sedimentary basins, as discussed later. The 20 sec maps are also similar to one another, with the exception of the Rayleigh phase velocity map. The 20 sec Rayleigh group velocity and Love wave group and phase velocity maps are more similar to the 10 sec maps than the 20 sec phase velocity map. This is because, like the 10 sec results, these maps are mostly sensitive to the wave speeds within the crust. This similarity between these maps lends credence to the tomographic results at short periods.

As Figure 15b shows, the 20 sec Rayleigh wave phase velocity map has a substantial sensitivity to the mantle and is better correlated with intermediate period maps. Examples of results at intermediate periods are shown in Figure 13, which presents a comparison between the 25 sec Rayleigh wave phase speed and the 40 sec Rayleigh wave group speed maps. Figure 15c also shows that these two wave types have very similar vertical sensitivity kernels, both waves being predominantly sensitive to shear velocities in the uppermost mantle. The measurements, however, are entirely different. We view the similarity between these maps, therefore, as a confirmation of the procedure at intermediate periods.

The longest period map presented here is the 60 sec Rayleigh wave phase speed map shown in Figure 14a. This map possesses considerable sensitivity to the upper mantle to a depth of about 150 km. It is compared to the map for the same wave type computed from the 3-D model of *Shapiro and Ritzwoller* [2002] shown in Figure 14b. At large scales, the maps are similar both in the distribution and absolute value of velocity. The 3-D model is radially anisotropic, and the agreement of absolute levels indicates that the model appears to account for anisotropy accurately. The transition between the low velocities of the tectonically active western US and the stable eastern US craton are largely consistent between the 3-D model and the ambient noise result. There are a few discrepancies, however, particularly in Texas where the ambient noise indicates mostly low velocities but with high velocities in the western Texas pan-handle. The lowest velocities in both maps lie in northern Nevada and southern Oregon. Of course, smaller scale anomalies appear in the ambient noise map. In particular, very low velocity anomalies appear in the Salton Trough in southern California and west of the Rio Grande Rift in New Mexico. High velocities extend into the southeastern US, particularly in northern Mississippi.

The fit of individual dispersion measurements to the tomographic maps reveals more about the quality of the data. The first type of information is the variance reduction relative to a homogeneous model, which here is taken to be the average of the measurements at each wave type and period. Figure 16a shows the variance reduction for the Rayleigh and Love wave group and phase speed maps from 10 to 90 sec period. (Rayleigh wave maps above 70 sec and Love wave maps above 25 sec are created in order to extend these statistics to the longer periods.) The largest variance reductions are for the Rayleigh wave phase velocity measurements, which are above 90% for the entire period range. Below

20 sec period, a similar variance reduction is achieved by the Rayleigh wave group speed maps. Love wave variance reduction is mostly lower. Love wave results above about 25 sec period are of little meaning because the number of measurements is so low. For all wave types, the mean path length stays nearly the same (around 1800 km) for all periods. The variance reduction reflects the residual level after tomography, which is plotted both in time and velocity in Figure 16b,c. Rayleigh wave phase velocity residuals are between 2 and 3 sec across the whole band, and time residuals for the other waves are mostly between 6 and 10 sec. In particular, Rayleigh wave group velocity residuals are 2-3 times larger than the anomalies for Rayleigh phase velocity, consistent with the standard deviation of the phase velocity measurement being about half that for group velocity.

7. Discussion

Detailed interpretation of surface wave dispersion maps is difficult because their sensitivity kernels are extended in depth and for group velocities they actually change sign. We present a qualitative discussion of Figures 11 - 14 here, but a more rigorous interpretation must await a 3-D inversion, which is beyond the scope of this paper. Many of the features of the maps in Figures 11 - 14 are not surprising, as they represent structures on a larger spatial scale similar to those revealed by the earlier work of *Shapiro et al.* [2005], *Lin et al.* [2007b], and *Moschetti et al.* [2007] in the western US. The details of the maps and how they vary with period, particularly at longer period parts and in the eastern US, are entirely new, however.

Overall, the most prominent anomaly on all maps is the continental-scale east-west dichotomy between the tectonically active western US and the cratonic eastern US. This dichotomy is observed at all periods, so it expresses both crustal and mantle structures,

although its contribution tends to grow with increasing period, at least in a relative sense. In terms of smaller scale regional structures, lateral crustal velocity anomalies that manifest themselves in surface wave dispersion maps are largely compositional in origin, whereas the mantle anomalies are predominantly thermal, although volatile content may also contribute to low velocity anomalies in both the crust and mantle. The most significant shallow crustal lateral velocity anomalies are due to velocity differences between the sedimentary basins and surrounding crystalline rocks, which are more significant than velocity variations within the crystalline crust. Large-scale anomalies in the uppermost mantle correspond to variations in lithospheric structure and thickness, predominantly reflecting differences between the tectonic lithosphere of the western US and cratonic lithosphere of the eastern and central US. Regional scale anomalies reflect variations in the thermal state of the uppermost mantle and crustal thickness.

Below 20 sec period (i.e., Figures 11 and 12), the dispersion maps dominantly reflect low velocity anomalies caused by sedimentary basins. The sediment model of (*Laske and Masters* [1997]) is shown in Figure 17 for comparison, with several principal structural units identified. Isopach contours are superimposed in Figure 11 with a 1 km interval for reference. The 10 sec period maps reveal low velocity anomalies associated with sediments in the Great Valley (CV) of central California as well as the Salton Trough/Imperial Valley of southern California extending down into the Gulf of California (GC). Low velocity anomalies are also coincident with the Anadarko (AB) basin in Texas/Oklahoma and the Permian Basin (PB) in west Texas. The deep sediments in the Gulf of Mexico (GOM) produce the largest low velocity features. Other basins such as the Wyoming-Utah-Idaho thrust belt (TB) extending north to the Williston basin (WB) also are apparent. This fea-

ture is seen best on the Love wave group speed map (Figure 11c) which has the shallowest sensitivity (see Figure 15a). Rayleigh wave phase speed on the other hand has deeper sensitivity and the Williston basin is only vaguely seen as a relative low velocity feature in Figure 11b. The Appalachian Basin (ApB) also appears as a relative slow anomaly in all the maps, although it is less pronounced due to the generally higher wave speeds and older (hence faster) sediments in the eastern US. The Michigan Basin (MB) is not observed, probably because of the lower resolution in the central US than in west where station coverage is better.

Low wave speeds observed in the 10 sec maps for the Basin and Range (BR) or Pacific Northwest (PNW) are interesting considering the lack of deep sedimentary basins. These anomalies, therefore, are probably due to thermal or compositional anomalies within the crystalline crust rather than in the sediment overburden.

Many of the features of the 10 sec maps in Figure 11 are also seen in the 20 sec maps of Figure 12. The range of depth sensitivities for the 20 sec dispersion maps is broad (Figure 15), however, and the Rayleigh wave phase speed map (Figure 12b) is more like other intermediate period maps. In addition, the shallower and older basins are not observed and the Sierra Nevada (SN) high velocity anomaly emerges more clearly at 20 sec than at 10 sec period. High speed anomalies are observed in the Gulf of California, in contrast to the 10 sec maps, due to thin oceanic crust.

At intermediate periods (25 - 40 sec), waves are primarily sensitive to depths between 25 and 70 km; namely, the deep crust (in places), crustal thickness, and the uppermost mantle. The Rayleigh wave 25 sec phase speed map and the 40 sec group speed map have maximum sensitivities at about 50 km depth and similar kernels, as Figure 15 il-

lustrates. Thick crust will tend to appear as slow velocity anomalies and thin crust as fast anomalies, for example. The anomalies on the maps in Figure 13 are similar to one another, with a few exceptions. The low velocity anomalies through the Rocky Mountain Region (RM, Colorado, Wyoming, eastern Utah, southern Idaho) and the Appalachian Mountains (ApM, northern Alabama to western Pennsylvania) are probably the most prominent low velocity features and they reflect thicker crust than average. To focus on this further, the box identified in the western panel of Figure 13b is shown in greater detail in Figure 18. Over-plotted in this figure is the depth to Moho model of *Seber et al.* [1997] with a 2.5 km contour interval. In general, areas with thicker crust in Nevada, Utah, Idaho, Wyoming, and Colorado have slower wave speeds, as expected. The bone-shaped high velocity anomaly of eastern Nevada corresponds to thinner crust beneath the Great Basin. East of Colorado, however, crustal velocities are higher due to the east-west tectonic dichotomy of the US and the lithosphere thickens beneath cratonic North America, which partially compensate for the low velocities that result from the thick crust. For this reason, the low velocities beneath the Rocky Mountain region do not extend into the central US. Nevertheless, the low velocities of the Colorado Plateau probably also reflect elevated crustal temperatures in addition to thicker crust. High velocity anomalies along the coasts, in southern Arizona, and northwestern Mexico reflect thinner crust in these regions.

Not all low velocity anomalies at intermediate periods have their origin in thicker crust. In the Pacific Northwest (PNW) states of northern California, Oregon, and Washington, slow anomalies are probably caused by a warm, volatilized mantle wedge overlying the subducting Juan de Fuca Plate. These low velocities are not seen south of the Mendocino

triple junction where the Farallon slab is no longer present in the shallow mantle. Perhaps surprisingly, the effect of the Anadarko Basin (AB) in western Oklahoma persists to these periods. Figure 15c illustrates that at intermediate periods very shallow structures will have a contribution to surface wave speeds.

Some features differ between the 25 sec group speed and the 40 sec phase speed maps, however. We note two. First, the 40 sec phase speed map has low velocities extending east into Nebraska and South Dakota, whereas these features are more subdued on the 25 sec group speed map. Second, the 25 sec group speed map has a high velocity anomaly in Michigan which is largely missing on the 40 sec phase speed map, although Michigan does appear as a relatively fast feature in this map. These discrepancies are small, and overall the maps agree quite well.

Moving to mantle sensitivity, Figure 14a shows the phase speed map at 60 sec period. This wave is most sensitive to depths from 50 to 150 km and reveals features of mantle structure and lithospheric thickness, in contrast to the shallower sensitivity of maps in Figure 13. The cold, thick lithosphere beneath the cratonic core of the continent appears clearly as a fast anomaly in the central and eastern US, while the thinner lithosphere in the western United States appears as low velocities over a large area. The transition between the tectonic and cratonic lithosphere is similar in both maps, but the ambient noise map reveals more a stair-step latitudinal structure rather than the more continuous variation with latitude found in the 3-D model prediction. The lowest velocities of the map are in the high lava plains of southeast Oregon and northwest Nevada, which is believed to be the location of the first surface expression of the plume that currently underlies Yellowstone. Yellowstone itself is below the resolution of the maps presented

in this study. However, a low velocity anomaly does appear in the maps based on the Transportable Array component of EarthScope/USArray (*Moschetti et al.* [2007]; *Lin et al.* [2007b]). Very low velocities are also associated with the Sierra Madre Occidental in western Mexico, which is a Cenozoic volcanic arc.

8. Conclusions

We computed cross-correlations of long time sequences of ambient seismic noise to produce Rayleigh and Love wave empirical Green functions between pairs of stations across North America. This is the largest spatial scale at which ambient noise tomography has been applied, to date. Cross-correlations were computed using up to two years of ambient noise data recorded from March of 2003 to February of 2005 at ∼200 permanent and temporary stations across the US, southern Canada, and northern Mexico. The period range of this study is from about 5 sec to 100 sec. We show that at all periods and most azimuths across the US, coherent Rayleigh wave signals exist in ambient noise. Thus, ambient noise in this frequency band across the US is sufficiently isotropically distributed in azimuth to yield largely unbiased dispersion measurements.

Rayleigh and Love wave group and phase speed curves were obtained for every inter-station path, and uncertainty estimates (standard deviations) were determined from the variability of temporal subsets of the measurements. Phase velocity standard deviations are about half the group velocity standard deviations, on average. These uncertainty estimates and the frequency dependent signal-to-noise ratios were used to identify the robust dispersion curves, with total numbers changing with period and wave type up to a maximum of about 9000. Sufficient numbers of measurements (more than 2000) to perform surface wave tomography were obtained for Love waves between about 8 sec and

25 sec period and for Rayleigh waves between about 8 sec and 70 sec period. A subset of these maps are presented herein. Resolution (defined as twice the standard deviation of a 2-D Gaussian function fit to the resolution surface at each point) is estimated to be better than 100 km across much of the US at most periods, but it degrades at the longer periods and degenerates sharply near the edges of the US, particularly near coastlines. This resolution is unprecedented in a study at the spatial scale of this one.

In general, the dispersion maps agree well with each other and with known geological features and, in addition, provide new information about structures in the crust and uppermost mantle beneath much of the US. Inversion to estimate 3-D structure in the crust and uppermost mantle and to constrain crustal anisotropy are natural extensions of this work.

Acknowledgments. All of the data used in this research were downloaded either from the IRIS Data Management Center or the Canadian National Data Center (CNDC). This research was supported by a contract from the US Department of Energy, DE-FC52-2005NA26607, and two grants from the US National Science Foundation, EAR-0450082 and EAR-0408228 (GEON project support for Bensen).

References

Alsina, D., R. L. Woodward, and R. K. Snieder (1996), Shear wave velocity structure in North America from large-scale waveform inversions of surface waves, *Journal of Geophysical Research*, *101*(B7), 15,969–15,986.

Barmin, M., M. Ritzwoller, and A. Levshin (2001), A fast and reliable method for surface wave tomography, *Pure and Applied Geophysics*, *158*(8), 1351–1375.

Bensen, G. D., M. H. Ritzwoller, M. P. Barmin, A. L. Levshin, F. Lin, M. P. Moschetti, N. M. Shapiro, and Y. Yang (2007), Processing seismic ambient noise data to obtain reliable broad-band surface wave dispersion measurements, *Geophysical Journal International*, (169), 1239–1260.

Butler, R., et al. (2004), The Global Seismographic Network surpasses its design goal, *EOS Transactions*, *85*(23), 225–229.

Campillo, M., and A. Paul (2003), Long-range correlations in the diffuse seismic coda, *Science*, *299*(5606), 547–549.

Cho, K., R. Herrmann, C. Ammon, and K. Lee (2007), Imaging the upper crust of the Korean Peninsula by surface-wave tomography, *Bulletin of the Seismological Society of America*, *97*(1B), 198–207.

Derode, A., E. Larose, M. Campillo, and M. Fink (2003), How to estimate the Green's function of a heterogeneous medium between two passive sensors? Application to acoustic waves, *Applied Physics Letters*, *83*(15), 3054–3056.

Ekström, G., J. Tromp, and E. Larson (1997), Measurements and global models of surface wave propagation, *J. Geophys. Res*, *102*, 8137–8157.

Gerstoft, P., K. Sabra, P. Roux, W. Kuperman, and M. Fehler (2006), Greens functions extraction and surface-wave tomography from microseisms in southern California, *Geophysics*, *71*(4), 123–131.

Godey, S., R. Snieder, A. Villasenor, and H. M. Benz (2003), Surface wave tomography of North America and the Caribbean using global and regional broad-band networks: phase velocity maps and limitations of ray theory, *Geophysical Journal International*, *152*(3), 620–632.

Larose, E., A. Derode, M. Campillo, and M. Fink (2004), Imaging from one-bit correlations of wideband diffuse wave fields, *Journal of Applied Physics*, *95*(12), 8393–8399.

Larose, E., A. Derode, D. Clorennec, L. Margerin, and M. Campillo (2005), Passive retrieval of Rayleigh waves in disordered elastic media, *Physical Review E*, *72*(4), 46,607–46,607.

Laske, G., and G. Masters (1997), A global digital map of sediment thickness, *EOS Trans. AGU*, *78*, 483.

Levshin, A., V. Pisarenko, and G. Pogrebinsky (1972), On a frequency-time analysis of oscillations, *Ann. Geophys*, *28*(2), 211–218.

Levshin, A., M. Ritzwoller, and J. Resovsky (1999), Source effects on surface wave group travel times and group velocity maps, *Phys. Earth Planet. Int*, *115*, 293–312.

Lin, F., M. P. Moschetti, and M. H. Ritzwoller (2007a), Phase-velocity measurement of Rayleigh wave based on ambient noise seismology, *Geophys. J. Int.*, in preparation.

Lin, F., M. H. Ritzwoller, J. Townend, M. Savage, and S. Bannister (2007b), Ambient noise Rayleigh wave tomography of New Zealand, *Geophys. J. Int.*, 18 pages, doi:10.1111.

Lobkis, O. I., and R. L. Weaver (2001), On the emergence of the Greens function in the correlations of a diffuse field, *The Journal of the Acoustical Society of America*, *110*, 3011–3017.

Moschetti, M. P., M. H. Ritzwoller, and N. M. Shapiro (2007), Ambient noise tomography from the first two years of the USArray transportable array: Group speeds in the western US, *Geochem. Geophys. Geosys.*, in review.

Ritzwoller, M., N. Shapiro, M. Barmin, and A. Levshin (2002), Global surface wave diffraction tomography, *J. Geophys. Res*, *107*(B12), 2335–2348.

Ritzwoller, M. H., and A. L. Levshin (1998), Eurasian surface wave tomography- group velocities, *Journal of Geophysical Research*, *103*(B3), 4839–4878.

Sabra, K. G., P. Gerstoft, P. Roux, W. Kuperman, and M. C. Fehler (2005), Surface wave tomography from microseisms in Southern California, *Geophysical Research Letters*, *32*.

Seber, D., M. Vallvé, E. Sandvol, D. Steer, and M. Barazangi (1997), Middle East tectonics: Applications of Geographic Information Systems (GIS), *GSA Today*, *7*(2).

Shapiro, N., and M. Campillo (2004), Emergence of broadband Rayleigh waves from correlations of the ambient seismic noise, *Geophysical Research Letters*, *31*(7), 1615–1619.

Shapiro, N. M., and M. H. Ritzwoller (2002), Monte-Carlo inversion for a global shear-velocity model of the crust and upper mantle, *Geophysical Journal International*, *151*(1), 88–105.

Shapiro, N. M., M. Campillo, L. Stehly, and M. H. Ritzwoller (2005), High-resolution surface-wave tomography from ambient seismic noise, *Science*, *307*(5715), 1615–1618.

Snieder, R. (2004), Extracting the Greens function from the correlation of coda waves: A derivation based on stationary phase, *Physical Review E*, *69*(4), 46,610–46,610.

Spetzler, J., J. Trampert, and R. Snieder (2002), The effect of scattering in surface wave tomography, *Geophysical Journal International*, *149*(3), 755–767.

Stehly, L., M. Campillo, and N. Shapiro (2006), A study of the seismic noise from its long-range correlation properties, *Journal of Geophysical Research*, *111*(B10).

Trampert, J., and J. Woodhouse (1996), High resolution global phase velocity distributions, *Geophysical Research Letters*, *23*(1), 21–24.

van der Lee, S., and G. Nolet (1997), Upper mantle S velocity structure of North America, *J.Geophys.Res*, *102*(B10), 22,815–22,838.

Villasenor, A., Y. Yang, M. H. Riztwoller, and J. Gallart (2007), Ambient noise surface wave tomography of the Iberian Peninsula: Implications for shallow seismic structure, *Geophys. Res. Lett.*

Wapenaar, K. (2004), Retrieving the elastodynamic Green's function of an arbitrary inhomogeneous medium by cross correlation, *Physical Review Letters*, *93*(25), 254,301–254,301.

Weaver, R. L., and O. I. Lobkis (2001), Ultrasonics without a source: Thermal fluctuation correlations at MHz frequencies, *Physical Review Letters*, *87*(13), 134,301.

Yang, Y., M. Ritzwoller, A. Levshin, and N. Shapiro (2007), Ambient noise Rayleigh wave tomography across Europe, *Geophysical Journal International*, *168*(1), 259–274.

Yao, H., R. D. van der Hilst, and M. V. de Hoop (2006), Surface-wave array tomography in SE Tibet from ambient seismic noise and two-station analysis-I. Phase velocity maps, *Geophysical Journal International*, *166*(2), 732–744.

Yoshizawa, K., and B. Kennett (2002), Determination of the influence zone for surface wave paths, *Geophysical Journal International*, *149*(2), 440–453.

Table 1. Number of Rayleigh wave measurements rejected and selected prior to tomography at 10-, 16-, 25-, 50-, and 70-sec periods.

Period	10-sec	16-sec	25-sec	50-sec	70-sec
Total waveforms	18554	18554	18554	18554	18554
Distance rejections	421	864	1541	3398	4748
Group velocity rejections					
Stdev not computed or SNR < 15	10385	7972	7870	11250	11560
Stdev > 100 m/sec	445	564	1148	1589	995
Time residual rejection	182	222	104	32	29
Remaining group measurements	7121	8932	7891	2285	1222
Phase velocity rejections					
Stdev not computed or SNR < 15	10423	8003	7894	11275	11554
Stdev > 100 m/sec	355	676	1103	408	143
Time residual rejection	161	321	135	58	36
Remaining phase measurements	7194	8690	7881	3415	2073

Table 2. Same as Table 1 but for Love waves.

Period	10-sec	16-sec	25-sec
Total waveforms	18554	18554	18554
Distance rejections	421	864	1541
Group velocity rejections			
Stdev not computed or SNR $<$ 15	9787	7463	13810
Stdev $>$ 100 m/sec	1678	2211	1172
Time residual rejection	222	245	63
Remaining group measurements	6446	7771	1968
Phase velocity rejections			
Stdev not computed or SNR $<$ 15	9770	7438	13810
Stdev $>$ 100 m/sec	1834	4005	1114
Time residual rejection	200	166	94
Remaining phase measurements	6329	6081	1995

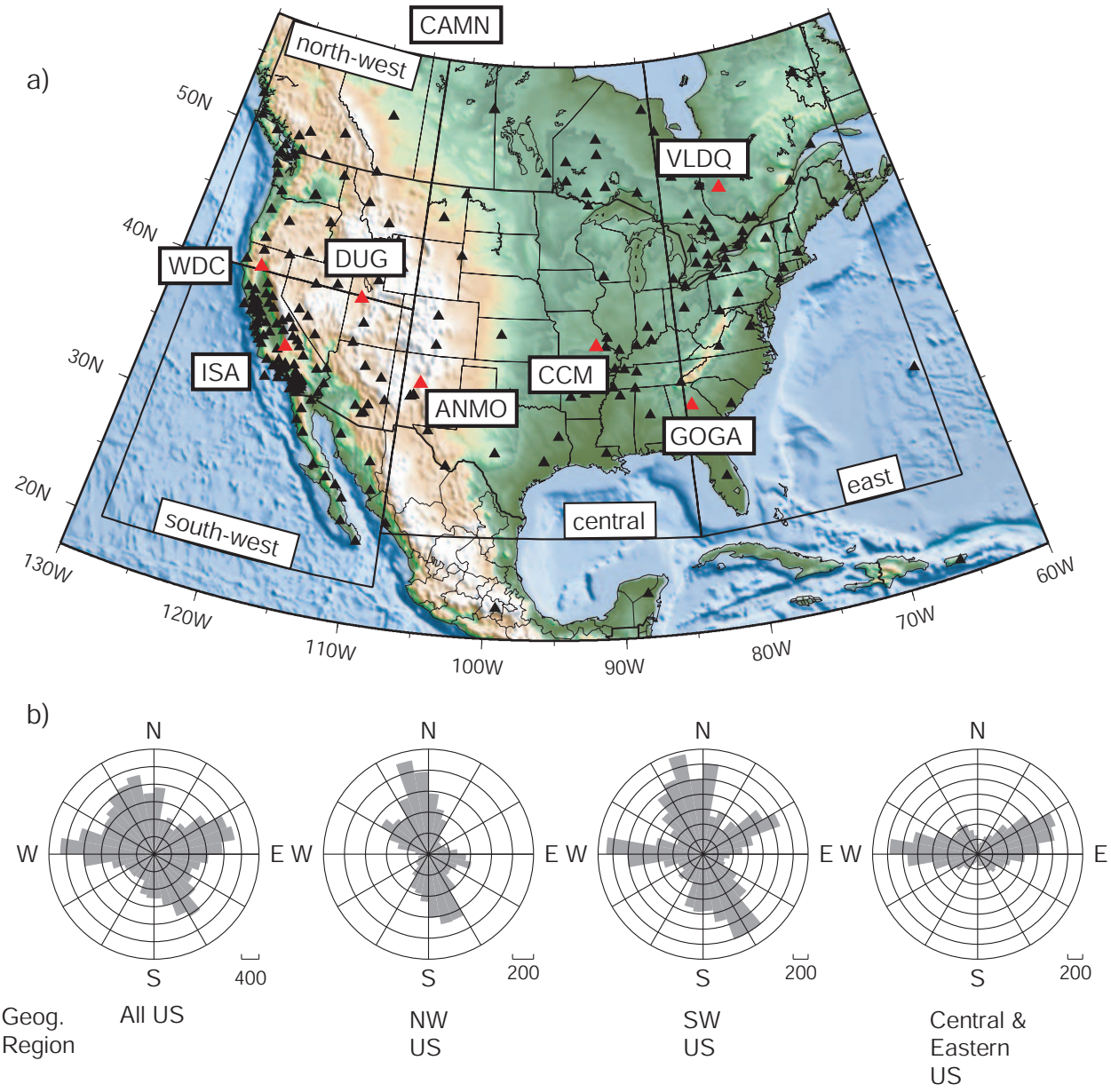

Figure 1. (a) The study area with stations represented as triangles. Red triangles with station names indicate inter-station paths for the waveforms and dispersion curves in Fig. 2. The study area is divided into four boxed sub-regions. (b) Azimuthal distribution of inter-station paths, plotted as the number of paths per 10° azimuthal bin, for the entire data set (at left) and in several sub-regions. Both azimuth and back-azimuth are included and indicate the direction of propagation of waves.

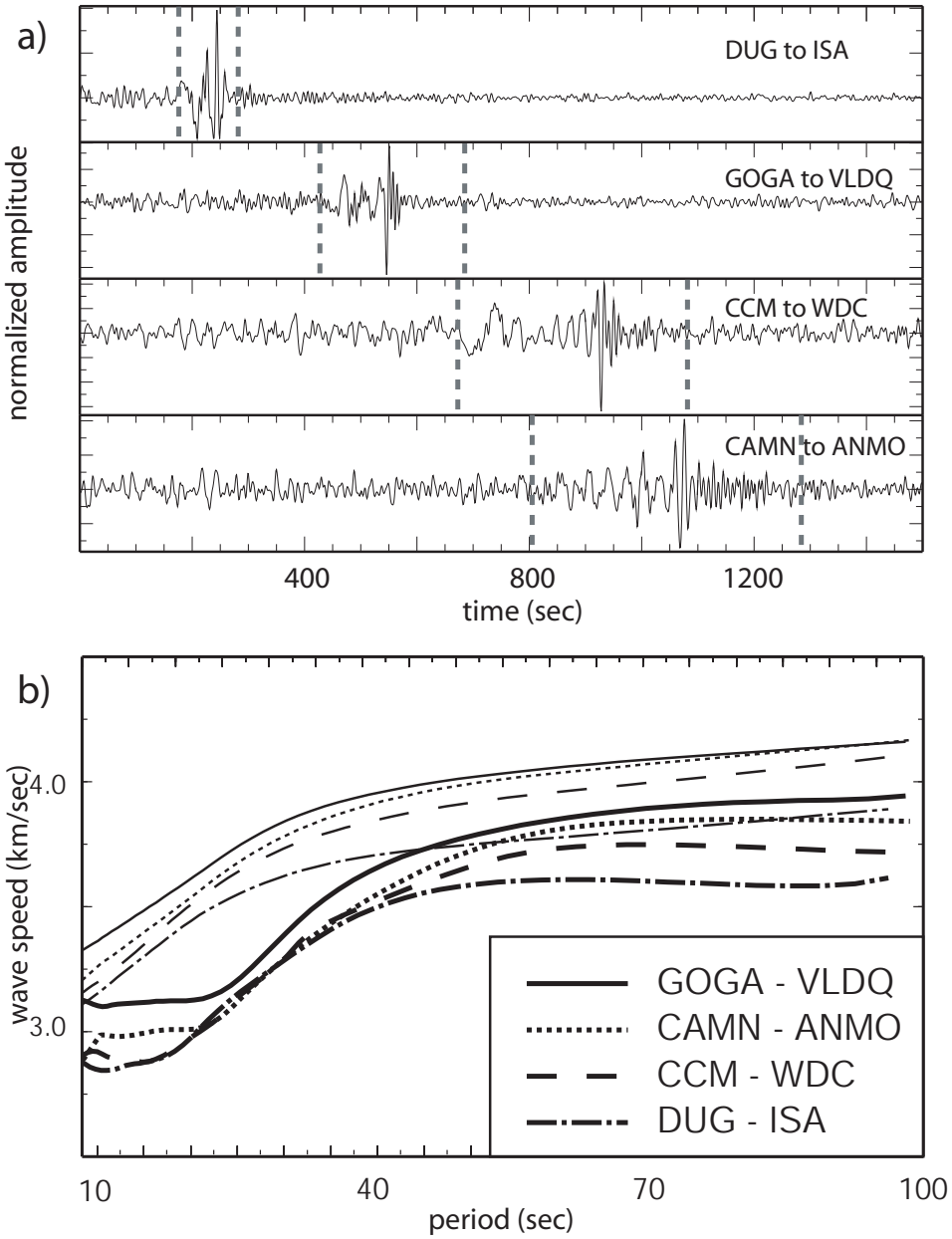

Figure 2. (a) Examples of broad-band vertical-component symmetric signal cross-correlations (Rayleigh waves) through various tectonic regimes for the inter-station paths indicated with red triangles in Fig. 1a. Waveforms are filtered between 7 and 100 seconds period. The time windows marked with vertical dashed lines are at 2.5 and 4.0 km/sec. (b) The corresponding group and phase speed curves. Group velocity curves are thicker than phase velocity curves.

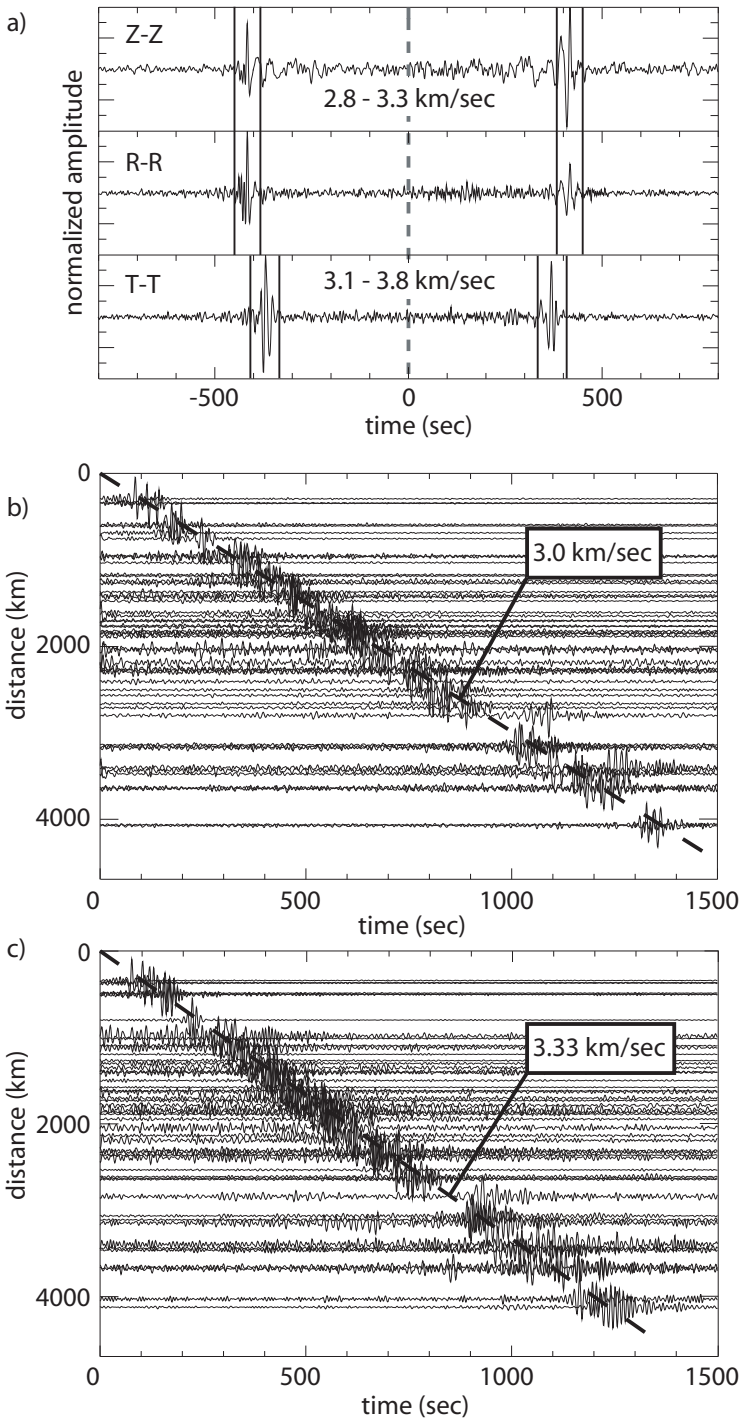

Figure 3. Example Rayleigh and Love wave empirical Green functions (EGFs). (a) Two-sided EGFs filtered between 5 and 50 seconds period for the stations CCM and RSSD. Rayleigh wave signals emerge on the Z-Z and R-R cross-correlations and are highlighted with a velocity window from 2.8 - 3.3 km/sec. Love waves are seen on the T-T component, identified with an arrival window from 3.1 - 3.8 km/sec. (b) Record section containing all cross-correlations between Z-Z components from GSN stations in the US separated by the

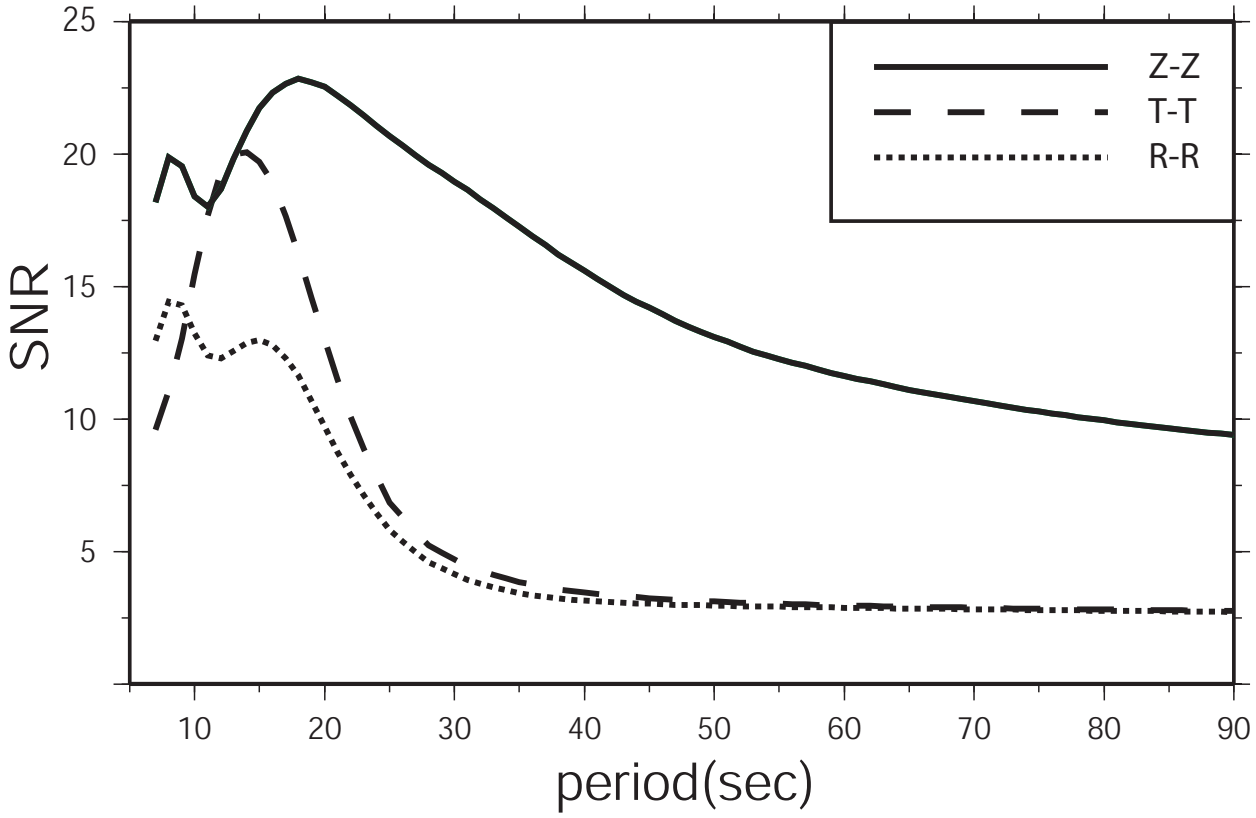

Figure 4. Relative signal quality represented as the average signal-to-noise ratio (SNR) for Rayleigh and Love waves computed using all stations in the study region. Rayleigh waves appear on vertical-vertical (Z-Z) and radial-radial (R-R) components, while Love waves are on the transverse-transverse (T-T) component cross-correlations.

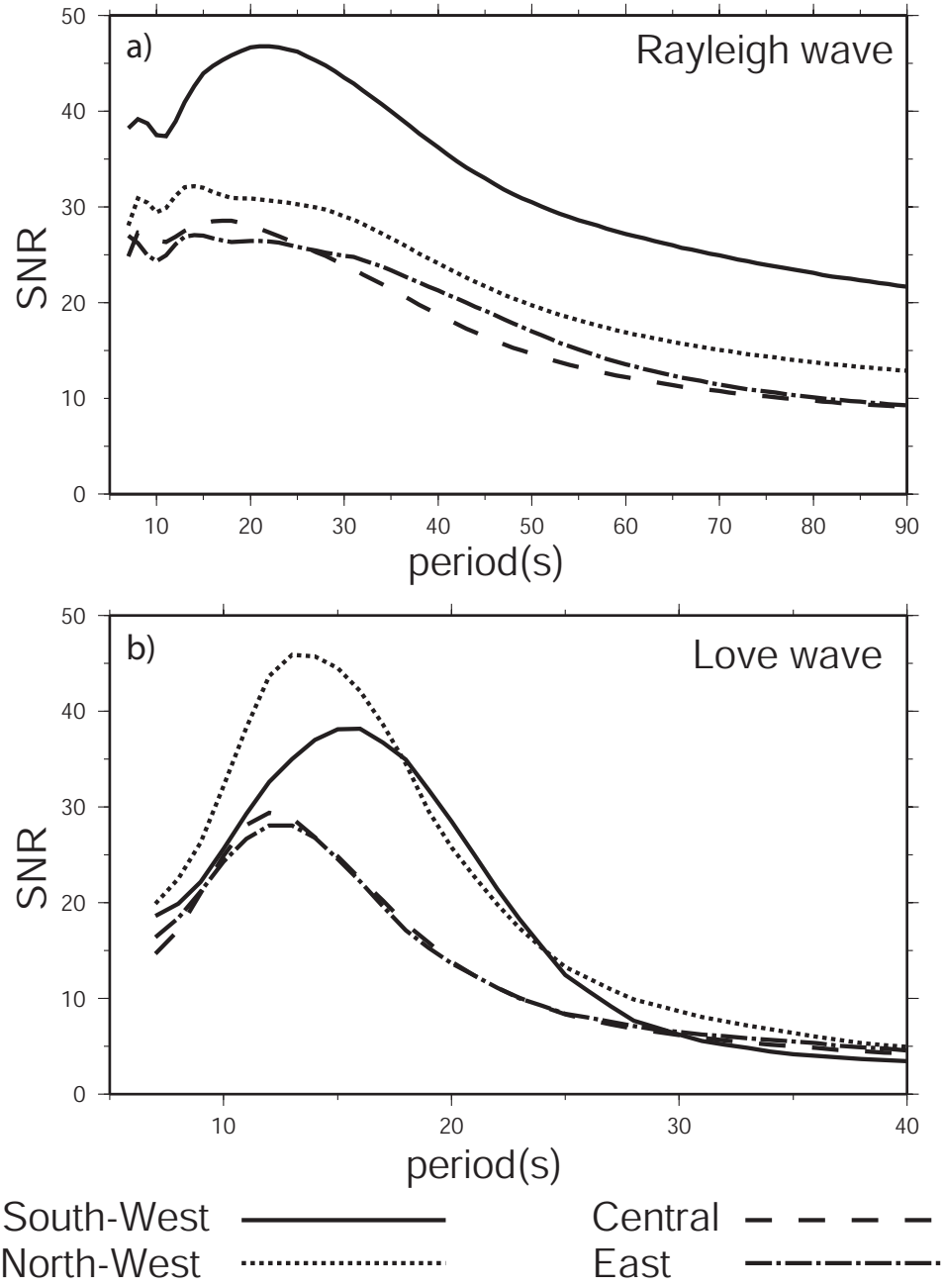

Figure 5. The mean signal-to-noise ratio is plotted versus period for (a) Rayleigh (Z-Z) waves and (b) Love (T-T) waves for the different geographical sub-regions defined in Fig. 1a. Note: the period bands for (a) and (b) differ.

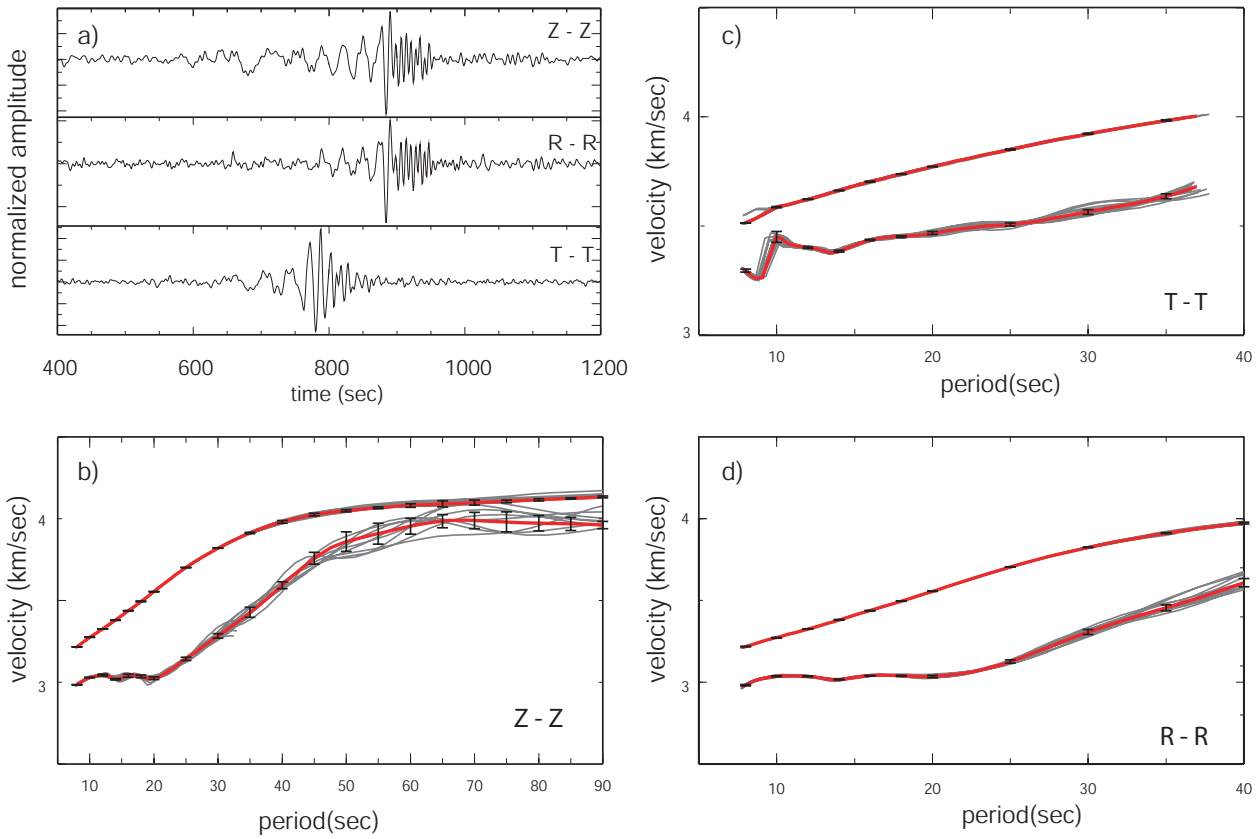

Figure 6. Illustration of the computation of measurement uncertainty. (a) Empirical Green functions on the Z-Z, R-R, and T-T components for the station pair DWPF and RSSD. (b) Measured Rayleigh wave group and phase speed curves from the Z-Z component empirical Green function. The 24-month measurements are plotted in red, individual 6-month measurements are plotted in grey, and the 1-σ error bars summarize the variation of the 6-month results. (c) Same as (b), but for the T-T component (Love waves). (d) Same as (b), but for the R-R component. Note the different period band and vertical scales in (b)-(d).

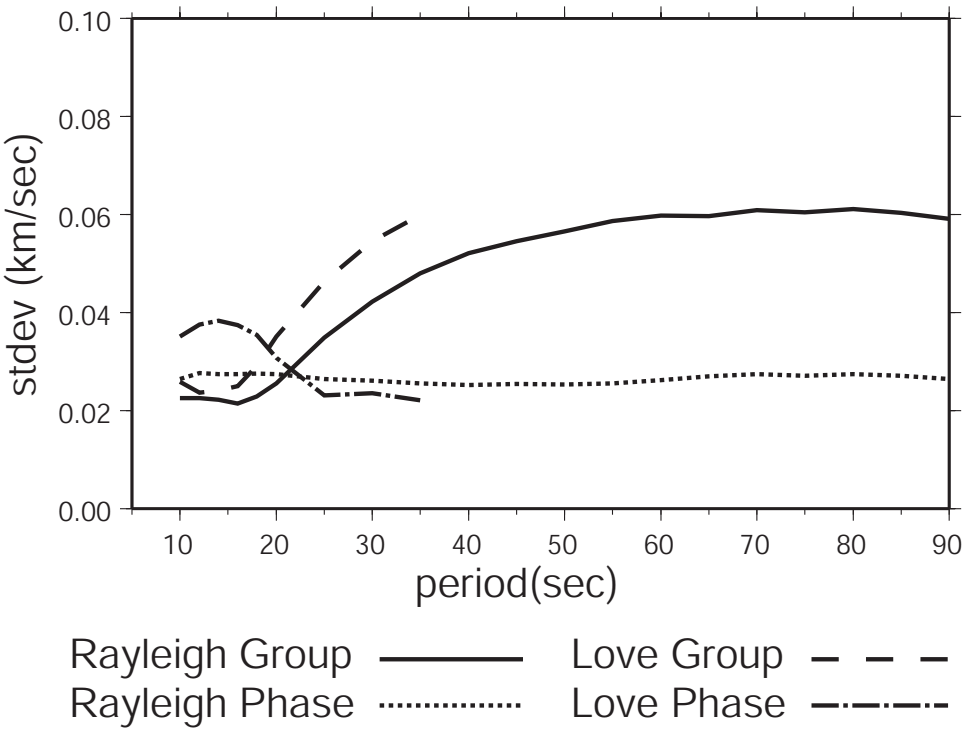

Figure 7. Average dispersion measurement standard deviation versus period for Rayleigh and Love wave group and phase speeds, where the average is taken over all acceptable measurements.

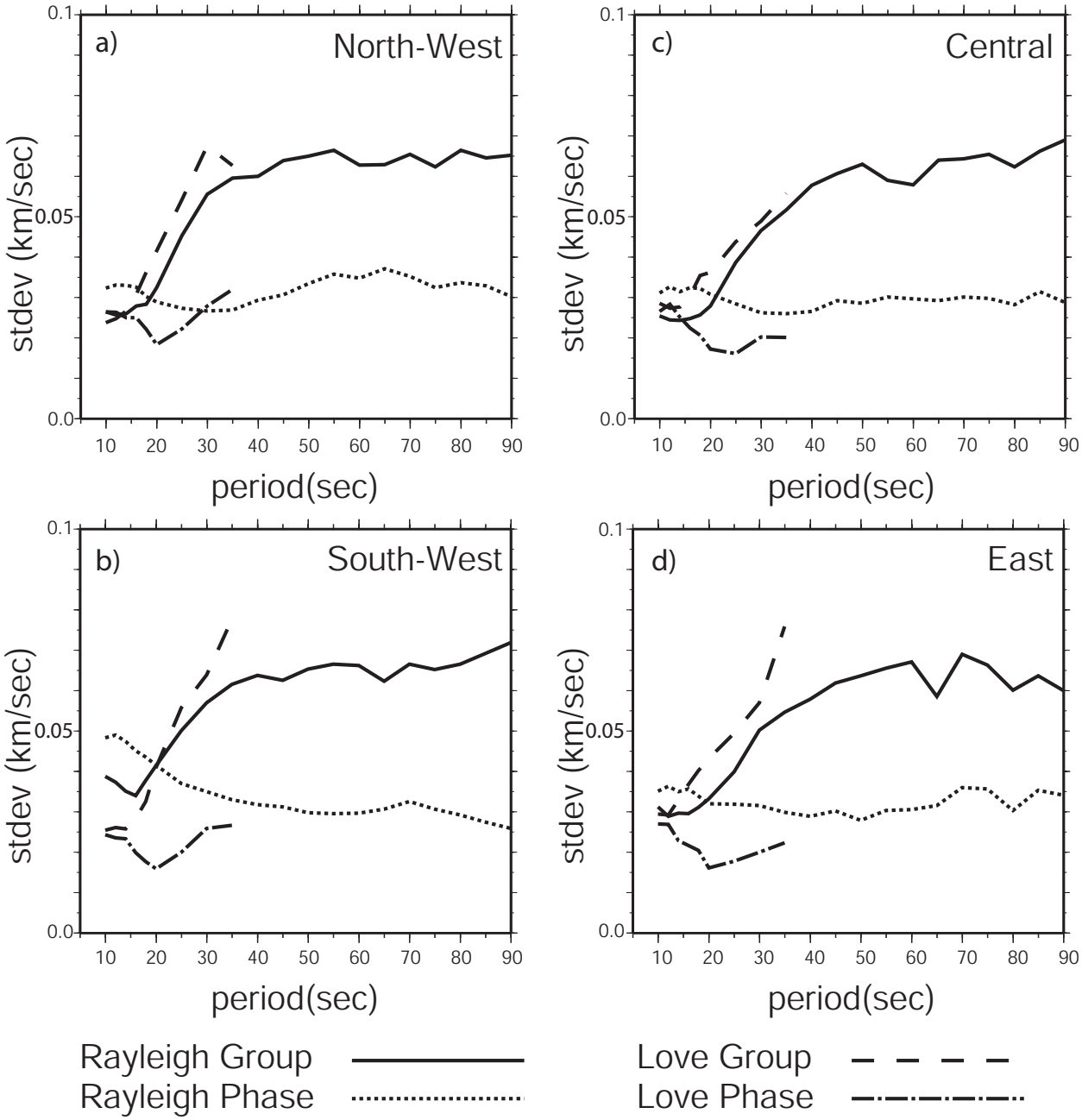

Figure 8. The average standard deviation of the velocity measurements as determined from the 6-month subsets of the data, averaged over all acceptable measurements. (a) - (d) Results are for the four sub-regions defined in Fig. 1a.

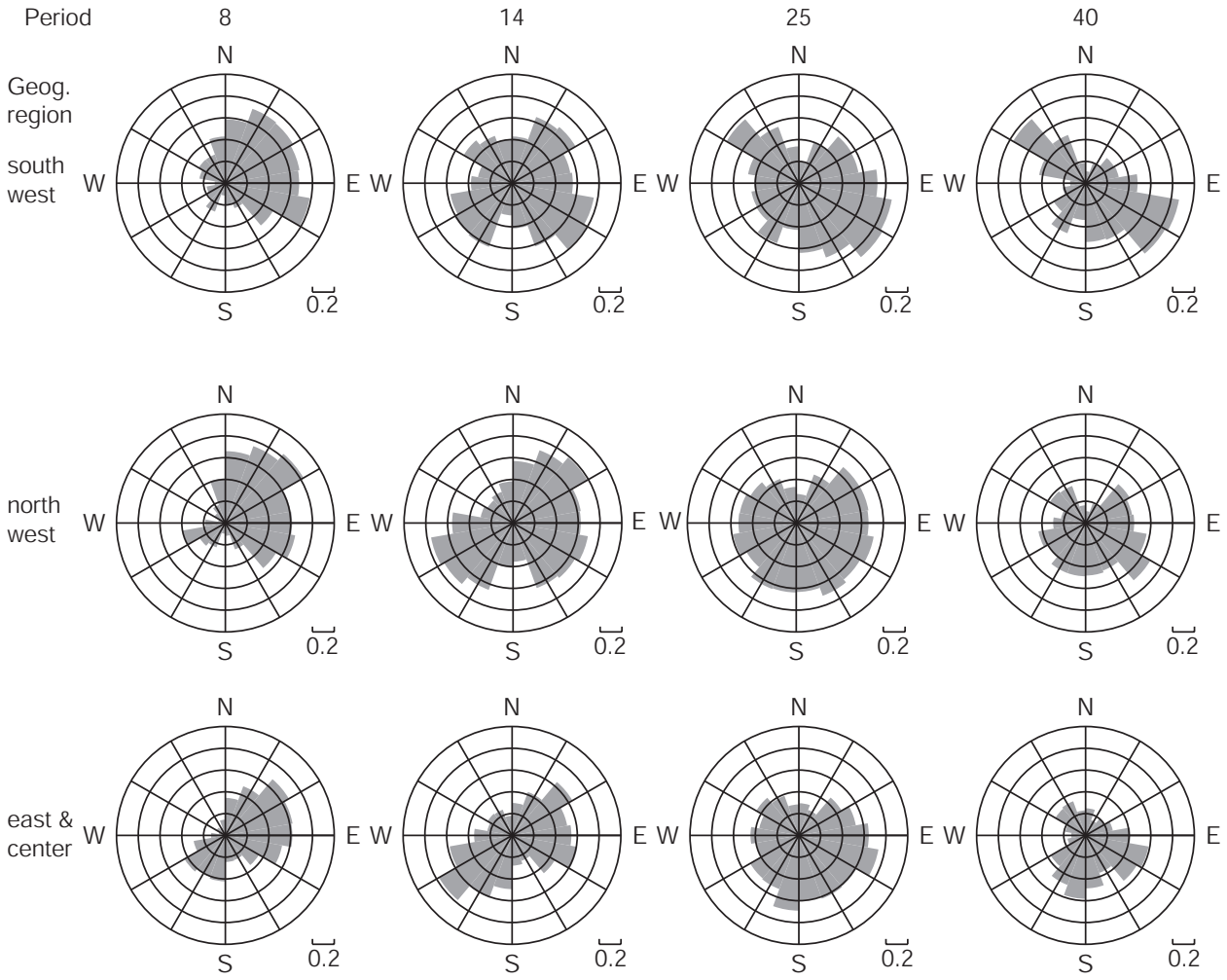

Figure 9. The directional dependence of high SNR (>10) Rayleigh wave cross-correlation signals plotted at different periods (8, 14, 25, 40 sec in different columns) and geographical sub-regions (different rows). Azimuth is the direction of propagation of the wave. Results are presented as fractions, in which the numerator is the number of inter-station paths in a particular azimuthal bin with SNR>10 and the denominator is the number of paths in the bin (from Fig. 1b).

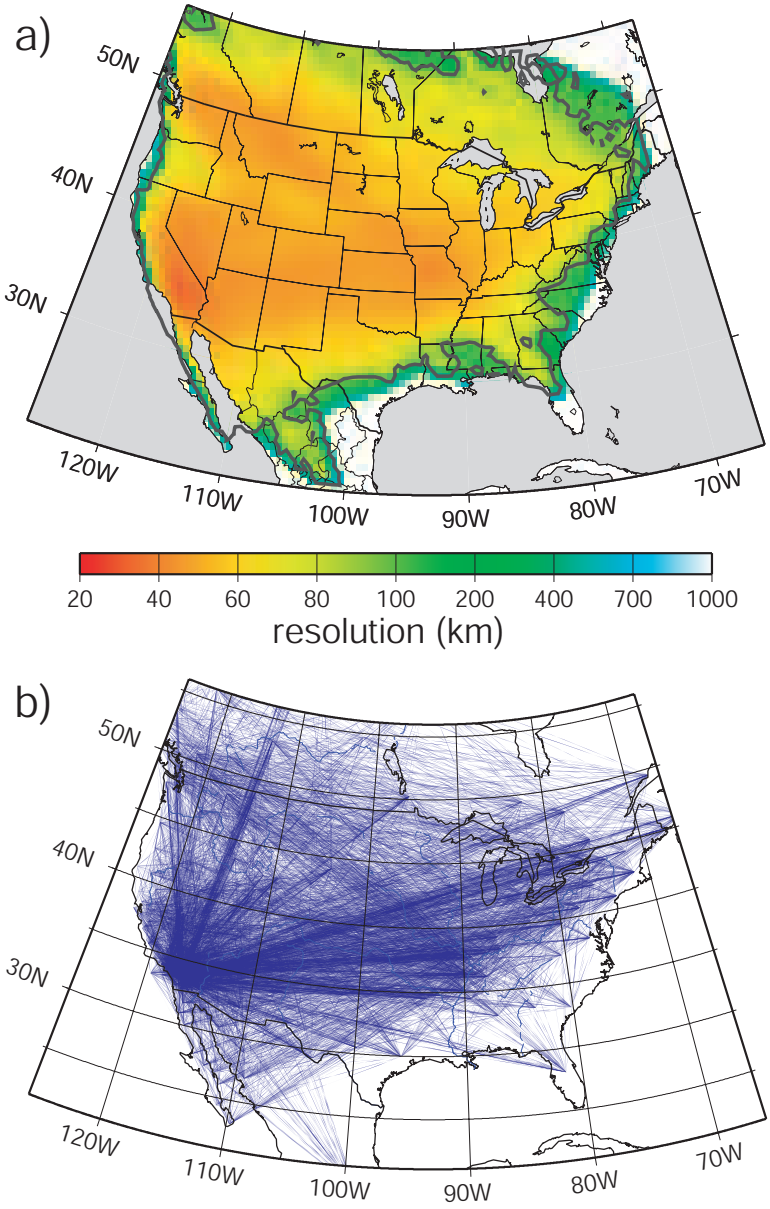

Figure 10. Path distribution and estimated resolution for the 10 sec period Rayleigh wave. (a) Resolution is defined as twice the standard deviation (2γ) of the 2-D Gaussian fit to the resolution surface at each point. The 200 km resolution contour is drawn and the color scale saturates at white when the resolution degrades to 1000 km, indicating indeterminate velocities. (b) Paths used to construct (a).

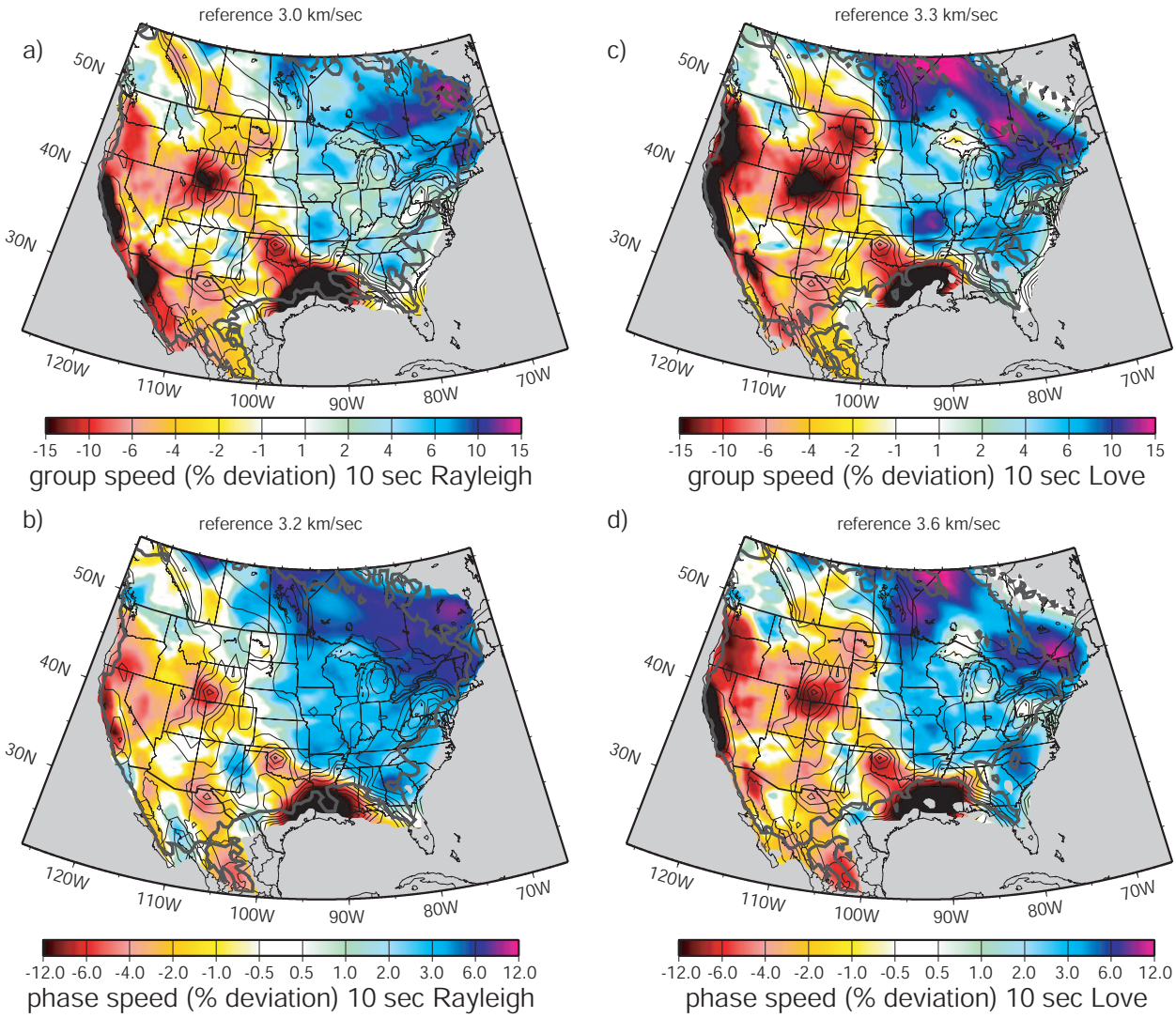

Figure 11. Rayleigh and Love wave group and phase speed dispersion maps at 10 sec period: (a) Rayleigh group speed, (b) Rayleigh phase speed, (c) Love group speed, and (d) Love phase speed. The thick grey contour outlines the region with better than 200 km resolution and areas with resolution worse than 1000 km are clipped to grey. Many sedimentary features labeled in Fig. 17 are visible and contours of the sediment model of *Laske and Masters* [1997] are plotted with thin black lines for reference. Note the differences is reference speeds and color scale ranges.

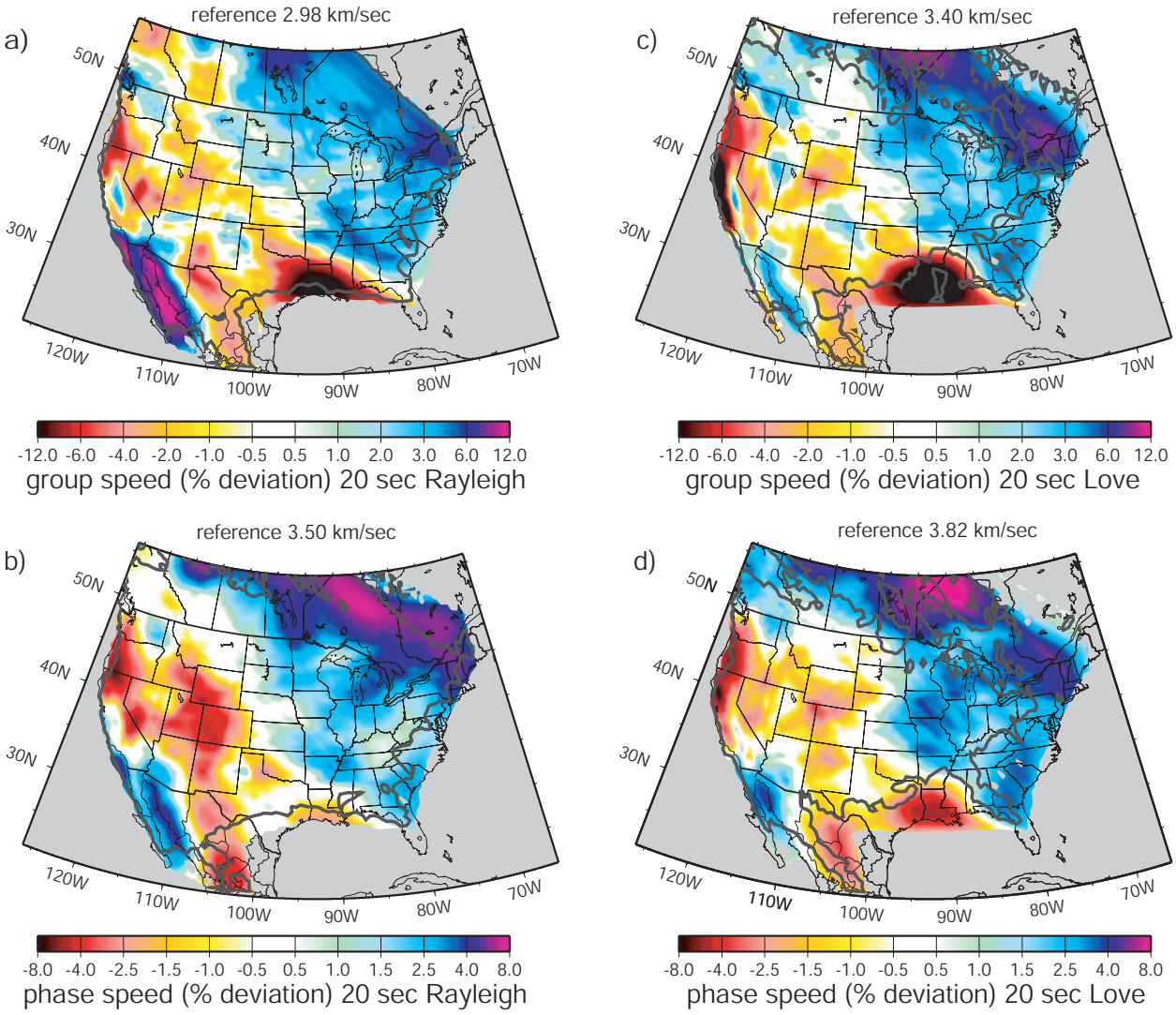

Figure 12. Same as Fig. 11, but for 20 sec period and sedimentary contours are suppressed.

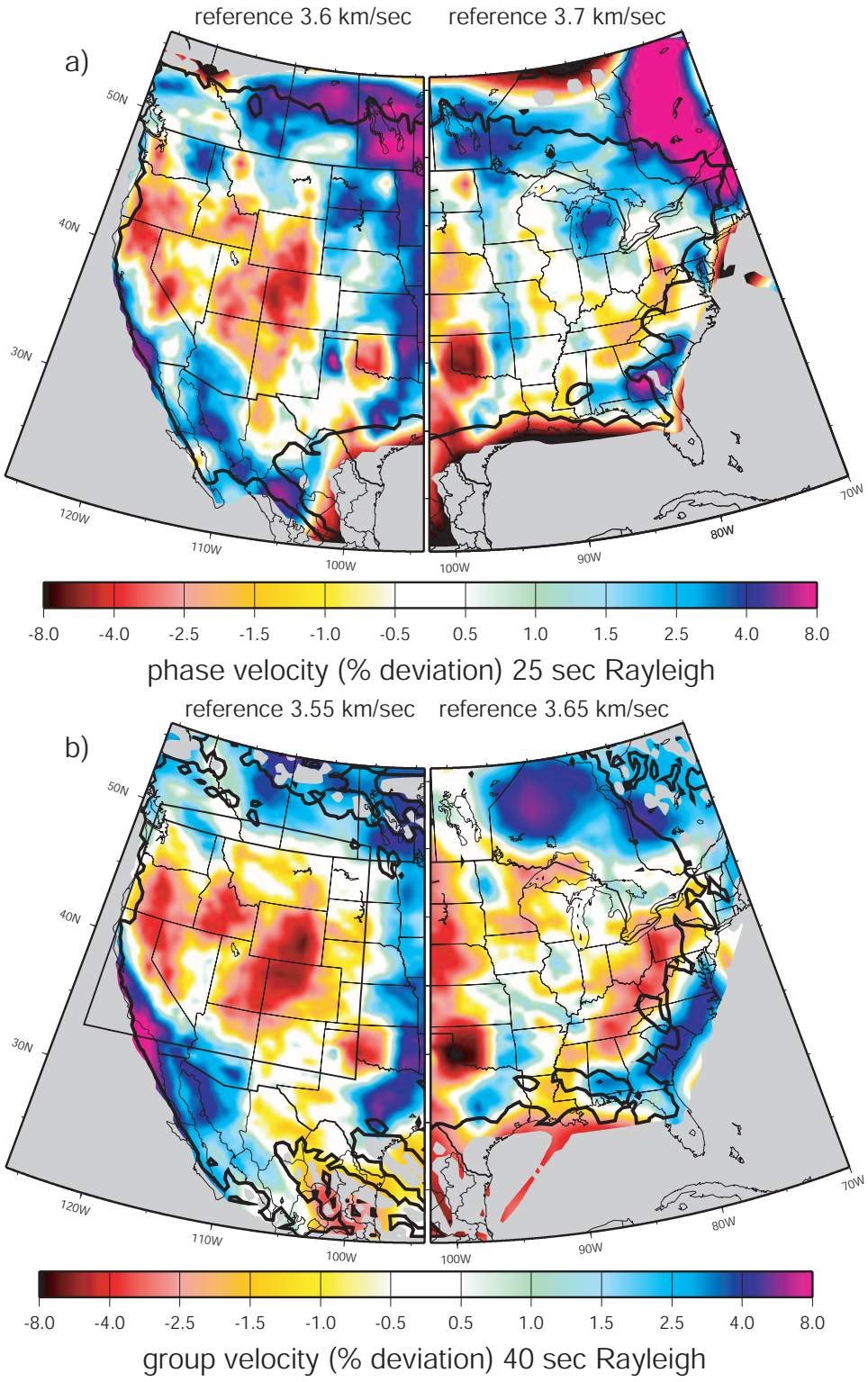

Figure 13. (a) The 25 sec period Rayleigh wave phase speed map. (b) The 40 sec Rayleigh wave group speed map. Grey contours indicate a resolution of 200 km and resolution less than 1000 km is colored grey. Different reference wave speeds are used in each half of the map and are indicated in the figure. The box in (b) corresponds to the region blown up in Figure 18.

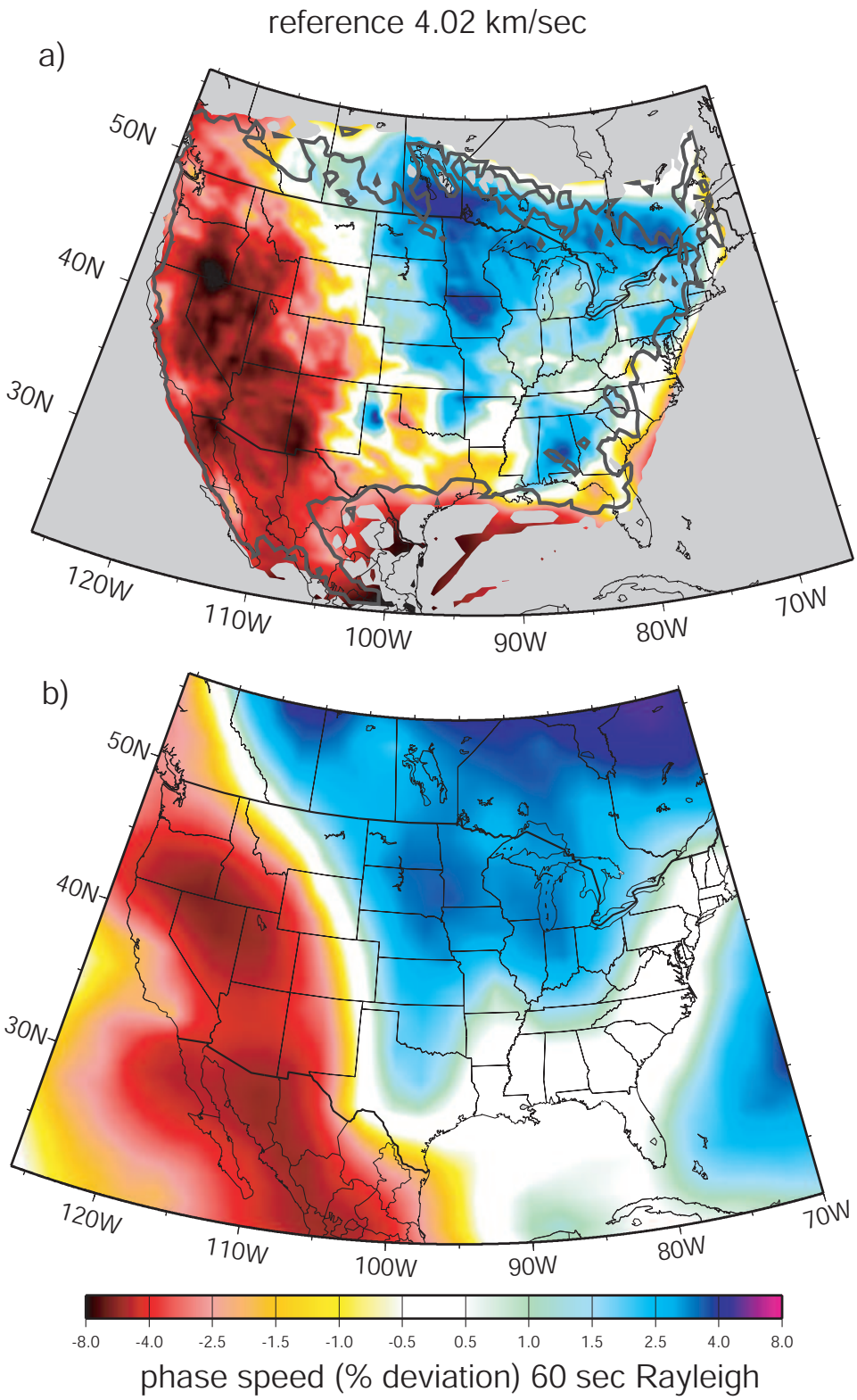

Figure 14. (a) The Rayleigh wave phase speed map at 60 sec period. The grey contour outlines the 200 km resolution and continental areas with indeterminate velocity are clipped to white. (b) Th prediction from a 3-D global model (*Shapiro and Ritzwoller* [2002]) is shown for comparison.

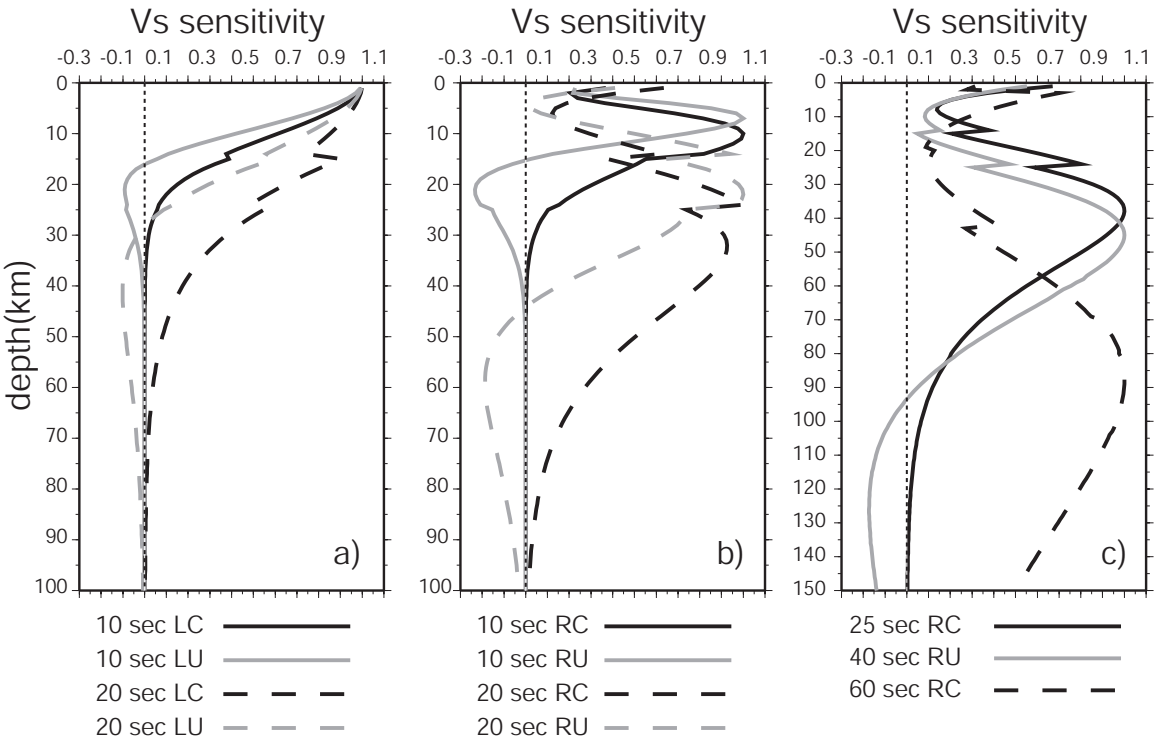

Figure 15. Sensitivity kernels for all dispersion maps shown here. The kernels have been normalized to have the same maximum amplitude and the labeling is as follows: RC - Rayleigh phase, RU - Rayleigh group, LC - Love phase, LU - Love group. Kernels are computed for PREM but with the ocean replaced by consolidated sediments.

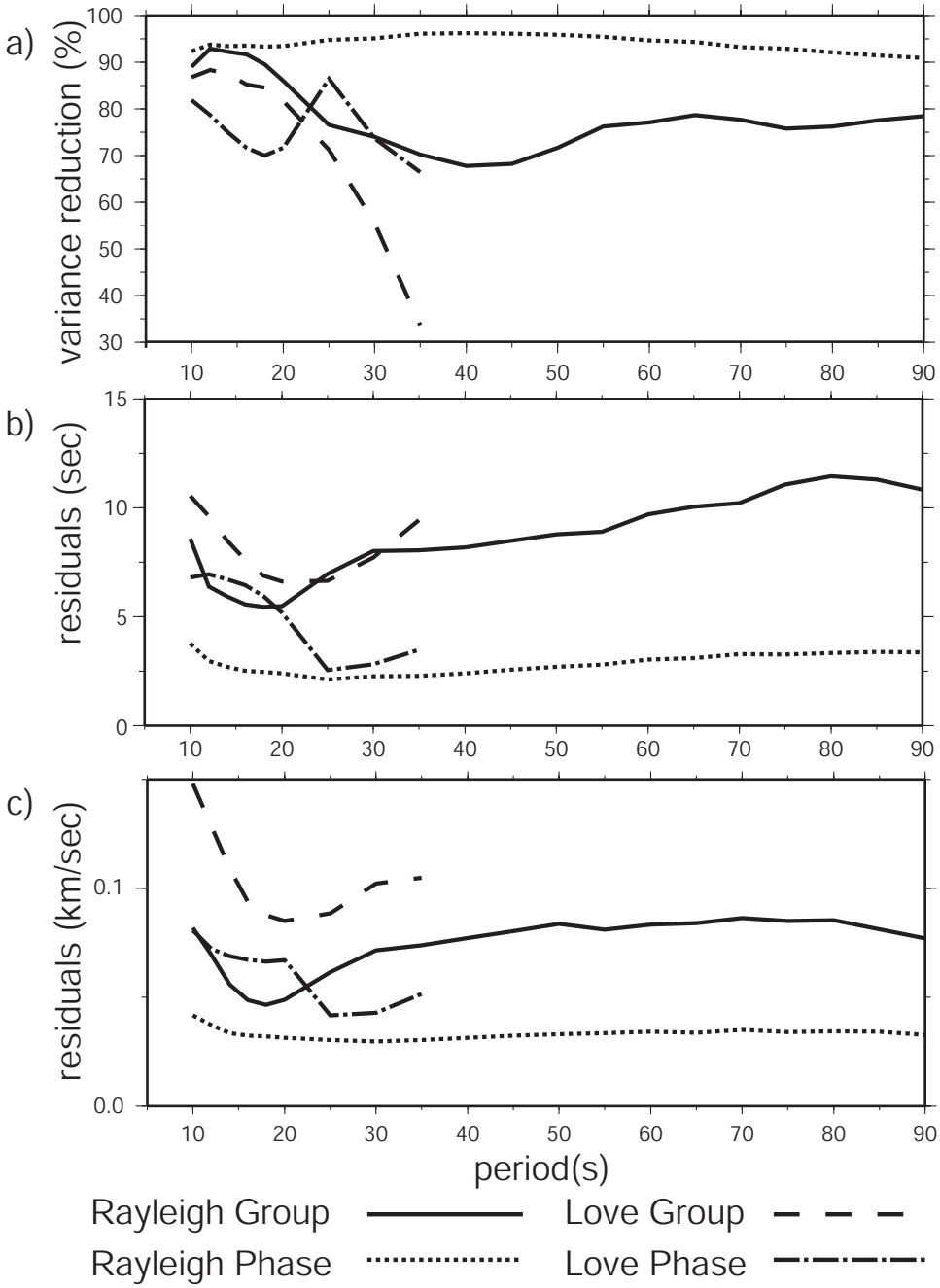

Figure 16. (a) Rayleigh and Love wave group and phase speed variance reduction as a function of period, computed relative to the mean measurement for each wave type and period. (b) The final travel-time residuals in seconds. (c) Final velocity residuals.

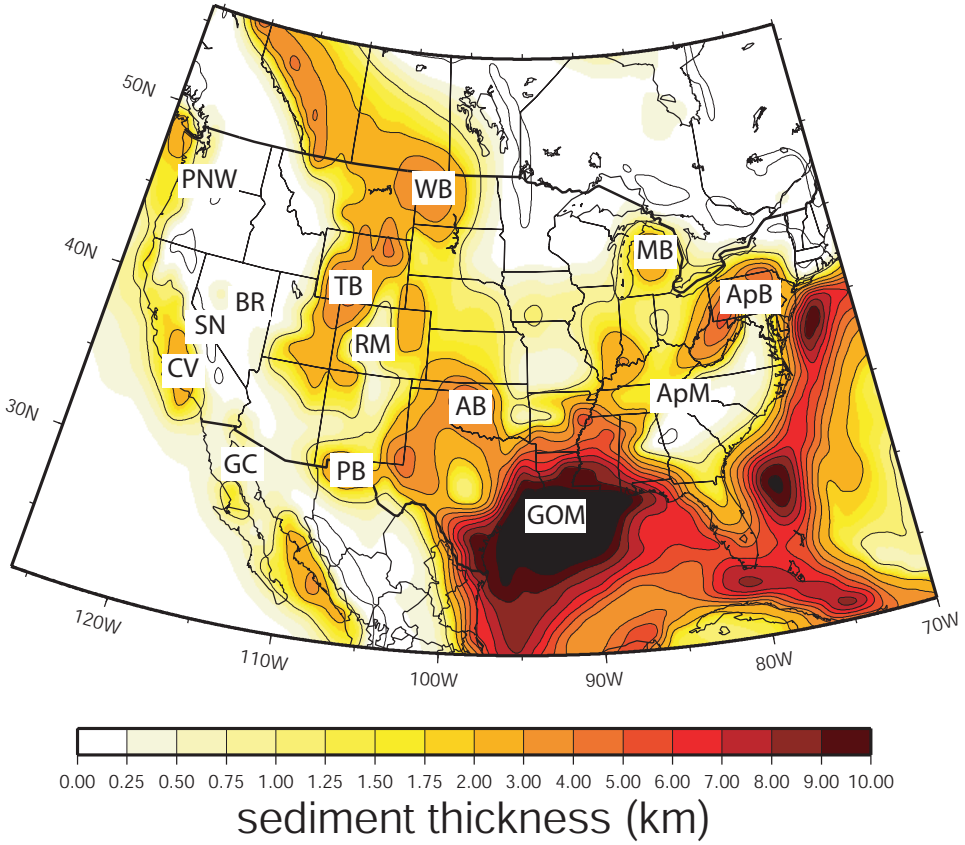

Figure 17. Sediment thickness model of *Laske and Masters* [1997] with several prominent basins and geographical features labeled: 'CV' - Central Valley in California, 'SN' - Sierra Nevada, 'AB' - Anadarko Basin, 'PB' - Permian Basin, 'GOM' - Gulf of Mexico, 'TB'- Wyoming-Utah-Idaho thrust belt, 'WB' - Williston Basin, 'ApB' - Appalachian Basin, 'MB' - Michigan Basin, 'BR' - Basin and Range, 'RM' - Rocky Mountain Region, 'ApM - Appalachian Mountains', 'PNW' - Pacific Northwest, 'GC' - Gulf of California.

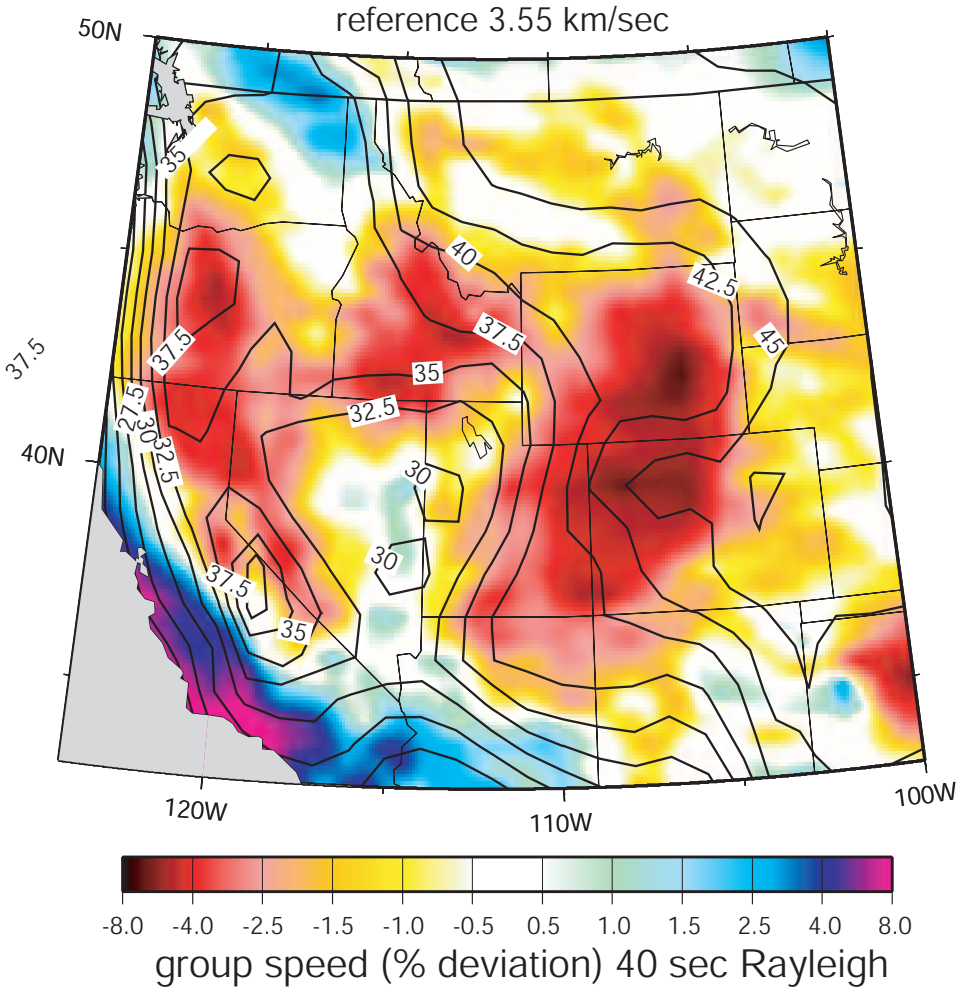

Figure 18. Rayleigh wave group speed dispersion map at 40 sec period for the region outlined in Fig. 13b. The Cornell US Moho depth model (*Seber et al.* [1997]) is plotted as contours with a 2.5 km contour interval with a maximum thickness under Colorado of 47 km. Low velocities generally correspond to thick crust.